Airfoil characteristics for wind turbines

Bak, Christian; Fuglsang, P.; Sørensen, Niels N.; Aagaard Madsen , Helge; Shen, W.Z.; Sørensen, Jens Nørkær

Publication date:
1999

Document Version
Publisher's PDF, also known as Version of record

Risø-R-1065(EN)

Airfoil Characteristics for Wind Turbines

Christian Bak, Peter Fuglsang, Niels N. Sørensen, Helge Aagaard Madsen
Risø National Laboratory

Wen Zhong Shen, Jens Nørkær Sørensen
Technical University of Denmark

Risø National Laboratory, Roskilde
March 1999

Abstract

Airfoil characteristics for use in the Blade Element Momentum (BEM) method are derived by use of systematic methods. The characteristics are derived from data on Horizontal Axis Wind Turbines (HAWT). The investigation and derivation of the airfoil characteristics are based on four different methods: 1) Inverse momentum theory, 2) Actuator disc theory, 3) Numerical optimisation and 4) Quasi-3D CFD computations.

The two former methods use as input 3D CFD computations and wind tunnel measurements on a 41-m full-scale rotor with LM 19.1 blades. The derived airfoil characteristics show that the maximum lift coefficient at the tip is low and that the maximum lift coefficient is high at the root compared to 2D airfoil characteristics. The use of the derived characteristics in aeroelastic calculations shows good agreement with measurements for power and flap moments. Furthermore, a fatigue analysis shows a reduction in the loads of up to 15 % from load calculations with the derived airfoil characteristics compared with a commonly used set of airfoil characteristics.

The numerical optimisation is based on both the 3D CFD computations and measurements on a 41-m rotor with LM 19.1 and LM 19.0 blades, respectively. The method requires measurements or CFD calculations of power and loads from a turbine and is promising since a set of lift and drag curves is derived that can be used to calculate mean values of power and loads. The maximum lift at the tip is low and at the root it is high compared to 2D airfoil characteristics. In particular the power curves were well calculated by use of the optimised airfoil characteristics.

In the quasi-3D CFD computations, the airfoil characteristics are derived directly. This Navier-Stokes model takes into account rotational and 3D effects. The model enables the study of the rotational effect of a rotor blade at computing costs similar to what is typical for 2D airfoil calculations. The depicted results show that the model is capable of determining the correct qualitative behaviour for airfoils subject to rotation. The method shows that lift is high at the root compared to 2D airfoil characteristics.

The different systematic methods show the importance of rotational and 3D effects on rotors. Furthermore, the methods show high maximum lift coefficients at the inboard part of the blade and low maximum lift coefficients at the outboard part of the blade compared to 2D wind tunnel measurements.

ISBN 87-550-2415-7
ISBN 87-550-2568-4 (internet)
ISSN 0106-2840

Information Service Department, Risø, 1999

Contents

List of symbols

a	Axial induction
a'	Tangential induction
B	Number of blades
c	Chord length
C_L	Lift coefficient
C_D	Drag coefficient
C_f	Skin friction coefficient
C_p	Pressure coefficient
C_x	Tangential force coefficient
C_y	Axial force coefficient
F	Tip loss factor
F_x	Tangential force pr. meter
F_y	Axial force pr. meter
F_{thrust}	Thrust force
k	Parameter in B-spline curve or turbulent kinetic energy
$k=z/c$	Non-dimensional spanwise distance
L_m	Measured power or load
L_c	Calculated power or load
M	Flap moment
p	Static pressure
P	Mechanical power or total pressure
P_{el}	Electrical power
r	Local radius
R	Rotor radius
$Re=Wc/\nu$	Reynolds number
T	Time or airfoil thickness
u	Velocity component in x-direction
v	Velocity component in y-direction
w	Velocity component in z-direction
V_0	Wind speed
W	Relative velocity of the flow around the airfoil
X	Cartesian co-ordinate
Y	Cartesian co-ordinate
Z	Cartesian co-ordinate
α	Angle of attack
ε	Turbulent dissipation
ϕ	Angle of the relative velocity W or 2D velocity potential
ν	Laminar viscosity
ν_t	Eddy viscosity
ω	Rotational frequency or vorticity
Ω_y	Angular velocity
ρ	Density
σ	Solidity of rotor

1 Introduction

Calculations of power and loads for wind turbines are mainly carried out using the Blade Element Momentum theory (BEM). In addition to operational conditions and blade geometry, the lift and drag coefficients for the airfoils used on the blades constitutes the input for this model.

The airfoil characteristics used in BEM are mostly based on 2D wind tunnel measurements on airfoils. However, a direct use of 2D wind tunnel measurements cannot reproduce the measured power. Such data are known to under-predict the forces acting on the blades in stalled conditions (Rasmussen, 1983). A likely explanation for the under-prediction is that the flow is not adequately modelled by static 2D airfoil data in the stalled regime.

From experiments, it is evident that radial flow exists in the bottom of separated boundary layers on rotating wings and it is likely that this alters the lift and drag characteristics of the individual airfoil section. The outflow induces a Corioles force in the chordwise direction, which acts as a favourable pressure gradient that tends to delay boundary layer separation. Himmelskamp (1945), who finds lift coefficients as high as 3 near the hub of a fan blade, first describes these 3D effects. Later, experiments are carried out by Milborrow and Ross (1984) in a wind tunnel study of the loading on a model rotor. They find that the effective lift coefficient is higher than that obtained from 2D data. These wind tunnel experiments are followed by a number of so-called field rotor experiments carried out in the period from 1985 to 1997. The experiments have all the same main objective, which is to quantify the influence of 3D and rotational effects on the airfoil characteristics of a rotating blade. The data, which now are stored in a common data base (Schepers et al., 1997) show the same overall influence of 3D and rotational effects. These effects are: 1) Increased post stall lift on the inboard part (30-40% radius) of the blade associated with increase in the drag, 2) Almost no negative slope of the post stall lift curve on the mid part of the blade and 3) Decreased lift in the tip region of the blade. The increased post stall lift on the inboard part of the blade seems to be caused by pressure distributions quite different from corresponding data from 2D flow. Although tufts on the surface indicate separation, a considerable suction can still be observed.

Using balanced wind vanes, Savino and Nyland (1985) make it possible to visualise the flow direction on the surface of a full-scale rotor. They find a chordwise flow upstream of the separation line, whereas the flow in the separated regions was radial. Experiments carried out by, e.g., Ronsten (1991) and Bruining et al. (1993) support these observations. In an analysis by Fogarty (1951), it is shown that 3D cross flow effects are small for attached boundary layers on a rotating blade. As a conclusion, Fogarty suggests that the deviations from 2D behaviour observed only occur for separated boundary layers. From flow visualisations on a rotating blade, McCroskey (1971) notes the same. He observes separated flow to be dominated by a significant radial flow component, whereas the location of the separation line does not change appreciably.

The existence of 3D and rotational effects in stalled conditions has lead to a correction of the 2D wind tunnel measurements to reproduce the correct power. This correction is based on qualified estimations and experiences rather than a

systematic derivation. Furthermore, different sets of airfoil coefficients are often used for the same rotor.

This report describes different systematic methods and the results for derivation of airfoil coefficients. The basis of the systematic methods is the forces acting on the blades. The forces are either determined from Computational Fluid Dynamics (CFD) or from measurements. Four different methods are used when deriving the airfoil coefficients:

1) Momentum theory,
2) Actuator disc theory,
3) Numerical optimisation and
4) Quasi-3D CFD computations.

The two former methods are described in chapter 2, the numerical optimisation method is described in chapter 3 and in chapter 4, the derivation using quasi-3D CFD computations is described. A discussion of the different systematic methods is presented in chapter 5 and conclusions are found in chapter 6.

2 Derivation by momentum theory and actuator disc theory

Two methods for deriving airfoil characteristics will be described in this chapter. The methods are based on 3D CFD calculated force distributions on the LM 19.1 blade with a 1.5-m root extender. The two methods require force distributions on the blades. Since standard measurements on a rotor only provide moments on the blades, this kind of determination of the loads cannot be used. Using the two methods based on 3D CFD calculations, a set of airfoil characteristics was derived for several radii on the blades. Finally, the derived airfoil characteristics were compared to 2D wind tunnel measurements.

2.1 3D CFD calculations

In the present work, an incompressible Navier-Stokes solver was applied to predict the power curve for a wind turbine. The only necessary inputs to the computations were the geometry of the blades and rotor, the wind speed in the farfield and the rotational speed.

In an earlier work, the Navier-Stokes solver was coupled to an actuator disc model in an iterative fashion (Hansen et al., 1997), in order to correct the velocities at the outer boundaries. In the present work, only a single solution of the Navier-Stokes problem on a relative large domain was necessary, and the correction at the outer boundaries for the presence of the rotor was accounted for using simple linear propeller theory.

Navier-Stokes Solver

The EllipSys3D General Purpose Navier-Stokes solver was used for solving the rotating blade problem. The code developed by Michelsen (1992, 1994) and Sørensen (1995) is a multi-block finite volume discretization of the Reynolds Averaged Navier-Stokes (RANS) equations in general curvilinear co-ordinates. The code uses simple variables (*u, v, w* and *p*) in a co-located storage arrangement, and Rhie/Chow (Rhie, 1981) interpolation is used in order to avoid odd/even pressure decoupling. For the rotor computations, a reference frame attached to the rotor was used, and the necessary fictitious forces were included in the momentum equations.

The convective terms are discretized using a second-order TVD upwind scheme implemented using the deferred correction approach first suggested by Khosla and Rubin (1974). Central differences are used for the viscous terms, where only the normal terms are treated fully implicit, while the terms from non-orthogonality and the variable viscosity terms are treated explicitly.

As we are working with the incompressible flow equations, no equations of state exist for the pressure. The necessary pressure/velocity coupling is obtained through the SIMPLE algorithm of Patankar and Spalding (1972). This method is based on deriving an equation for the pressure or pressure correction by combining the continuity equation with the momentum equations.

The equations are solved in an iterative manner. First, the momentum equations are used as a predictor to advance the solution in time. At this point in the computation, the resulting flow field will not fulfil the continuity equation. The re-written continuity equation (the so-called pressure correction equation) is used as a corrector making the predicted flow field satisfy the continuity constraint. This two step procedure corresponds to a single iteration or pseudo time step, and the process is repeated until a convergent solution is obtained.

The three momentum equations are solved de-coupled using a red/black Gauss-Seidel point solver. The solution of the Poisson system arising from the pressure correction equation is accelerated using a multi-grid method. In order to accelerate the overall algorithm, a three level grid sequence and local time stepping are used.

In the present work, the turbulence in the boundary layer was modelled by the k-ω SST eddy viscosity model by Menter (1993). The details of the model will not be given here. It will only be stated that the model was chosen because of the very promising results for 2D separated flows (Wilcox, 1994, Menter, 1992). The equations for the turbulence model were solved after the momentum and pressure correction equations in every iteration/pseudo time step.

Geometry and Computational Mesh

A three-bladed rotor identical to the one used on the Nordtank NTK 500/41 turbine was investigated in the present work. The rotor was equipped with three LM19.1 blades, the rotor diameter was 41 meters, and the rotational speed was 27.1 RPM. In the present investigation, the pitch angle was set to zero.

As the turbine was an upwind turbine, the influence of the tower and nacelle on the rotor aerodynamics could be neglected to a first approximation. This highly simplified the geometrical complexity of the problem, and the 1P interference with the tower and nacelle was avoided by this simplification. By additionally neglecting the vertical shear in the wind profile, the flow over the rotor was fully steady in a global sense, and the blades experienced the same conditions irrespectively of the actual position of the rotor. Dynamic effects from local flow separation could nevertheless cause the flow to be unsteady.

These underlying simplifications resulted in the following simpler problem where only the rotor needed to be modelled, and the flow over the rotor was assumed steady. In the present work, only one of the blades was explicitly modelled in the actual computations. The remaining blades were accounted for using periodic boundary conditions, exploiting the 120 degrees symmetry of the three bladed rotor.

A multi-block mesh was constructed around the rotating blade. For the region near the individual blades, we used an O-configuration in the chordwise direction and an H-configuration in the spanwise direction. Stacking and bending meshes generated by a 2D hyperbolic/transfinite mesh generator giving nearly orthogonal meshes near the blade surface generated this section. In the axial direction, this section of the mesh extended 3/4 rotor diameters up and down-stream. In the directions up- and down-stream of the rotor plane, the O-H-section was extended using a polar grid, placing the up- and down-stream boundary of the domain ~ 6 rotor radii away from the rotor plane. The mesh covered a 120 degrees section of the three-bladed rotor, the remaining 240 de-

grees were accounted for through use of periodic boundary conditions, see Figure 2-1 and Figure 2-2.

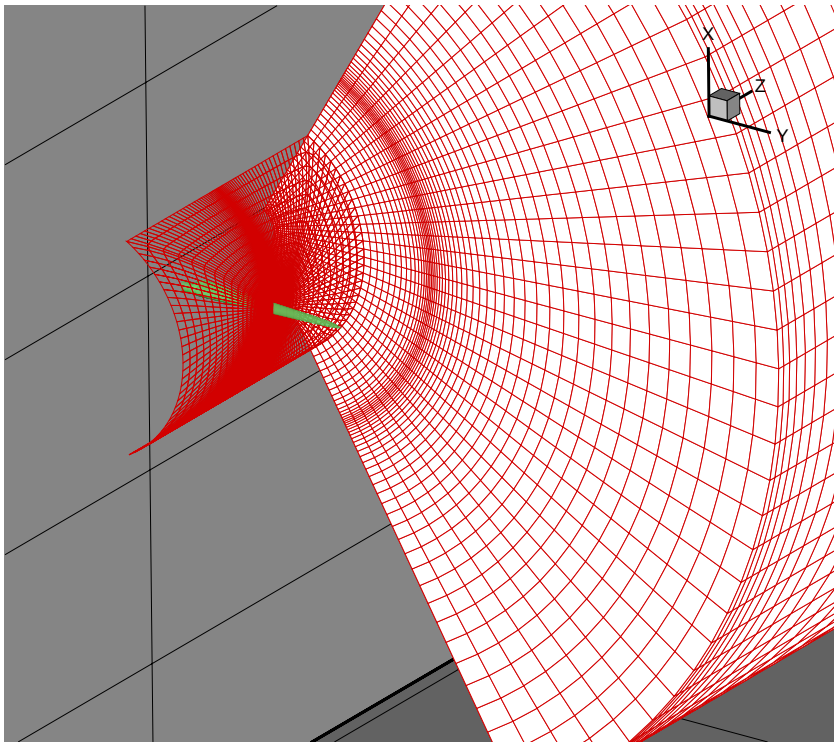

Figure 2-1 Mesh of the 120 degrees section of the three-bladed rotor. The blade is seen to the left and the outer boundary is seen to the right.

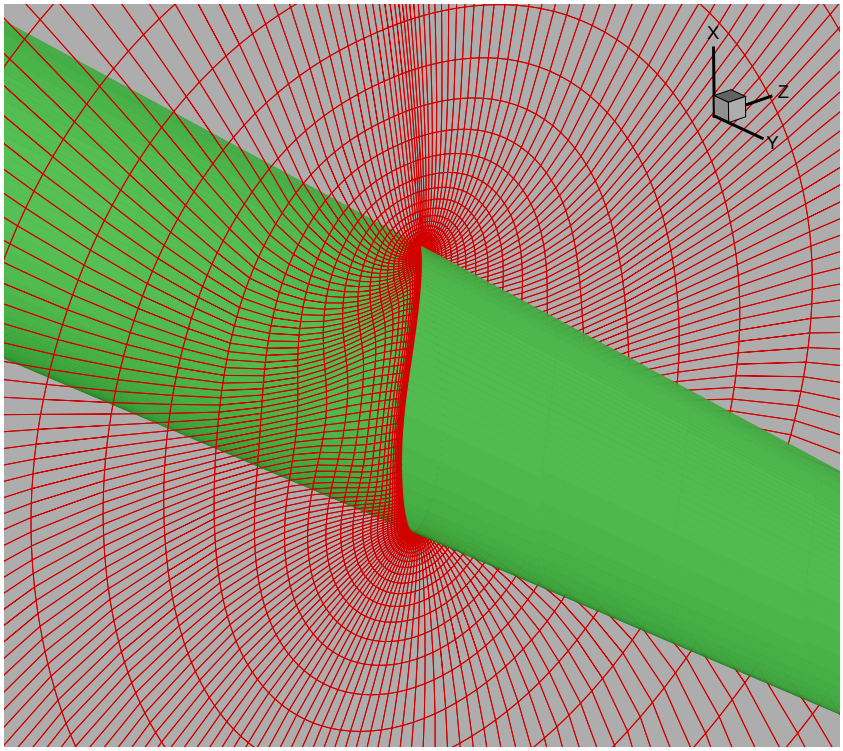

Figure 2-2 A view of an O-mesh around an airfoil section on the blade.

The meshes had 192 cells distributed on the blade in the chordwise direction, 32 cells along the blade in the spanwise direction, and a normalised distance to the first internal point of $y^+ \sim 2$. The mesh contained approximately 900.000 cells.

Boundary Conditions

Farfield boundary conditions derived from linear propeller theory were specified on the lid of the cylindrical domain upstream of the rotor plane and on the outer cylindrical part of the domain. Outlet conditions were enforced on the lid downstream of the rotor plane, approximating the flow to be fully developed. Explicit periodic conditions were specified in the direction of rotation. Slip conditions, assuring zero flow penetration, were specified at the inner cylindrical part of the domain. In addition, no-slip conditions were prescribed on the surfaces of the blades.

Although a very large domain was used for the present computations, the outer boundary was still significantly influenced by the presence of the rotor. This was especially true for low wind speeds, where the expansion of the rotor wake was large and the induced velocities were large compared to the wind speed.

The following procedure was used in every iteration to obtain the correct farfield boundary conditions.

First, the thrust of the rotor was computed as the number of blades times the thrust per blade:

$$T = N_{blades} \times T_{blade}, \qquad (2\text{-}1)$$

and the thrust of the blade was obtained by integrating the pressure distribution. Then the thrust coefficient was computed as:

$$C_T = \frac{T}{1/2 W_0^2 \pi R_{rotor}^2}. \qquad (2\text{-}2)$$

Having computed the thrust coefficient, the axial induction factor, *a*, could be computed from the following expression:

$$C_T = 4a(1-fa), f = \begin{cases} 1, & a < 1/3 \\ (5-3a)/4, & a \geq 1/3 \end{cases} \qquad (2\text{-}3)$$

Finally, the velocities at the boundaries were specified according to the following expressions for the points outside the slipstream:

$$\left.\begin{aligned} U &= \frac{1}{2} a W_0 \frac{R_{rotor}^2 x}{(R_{rotor}^2 + z^2)^{3/2}} \\ V &= \frac{1}{2} a W_0 \frac{R_{rotor}^2 y}{(R_{rotor}^2 + z^2)^{3/2}} \\ W &= W_0 - a W_0 (1 + \frac{z}{\sqrt{R_{rotor}^2 + z^2}}) \end{aligned}\right\} for \sqrt{x^2 + y^2} \le R_{wake,} \qquad (2\text{-}4)$$

and inside the slipstream:

$$\left.\begin{aligned} U &= \frac{1}{2} a W_0 \frac{R_{rotor}^2 x}{(x^2 + y^2 + z^2)^{3/2}} \\ V &= \frac{1}{2} a W_0 \frac{R_{rotor}^2 y}{(x^2 + y^2 + z^2)^{3/2}} \\ W &= \frac{1}{2} a W_0 \frac{R_{rotor}^2 z}{(x^2 + y^2 + z^2)^{3/2}} \end{aligned}\right\} for \sqrt{x^2 + y^2} < R_{wake}. \qquad (2\text{-}5)$$

In the previous expressions, the slipstream radius was approximated by the following expression:

$$R_{wake} = R_{rotor} (1 - \frac{az}{2\sqrt{R_{rotor}^2 + z^2}}). \qquad (2\text{-}6)$$

Based on the boundary conditions described, the result from the computations is shown Figure 2-3. The CFD computed power curve is compared to a measured power curve (Paulsen, 1995).

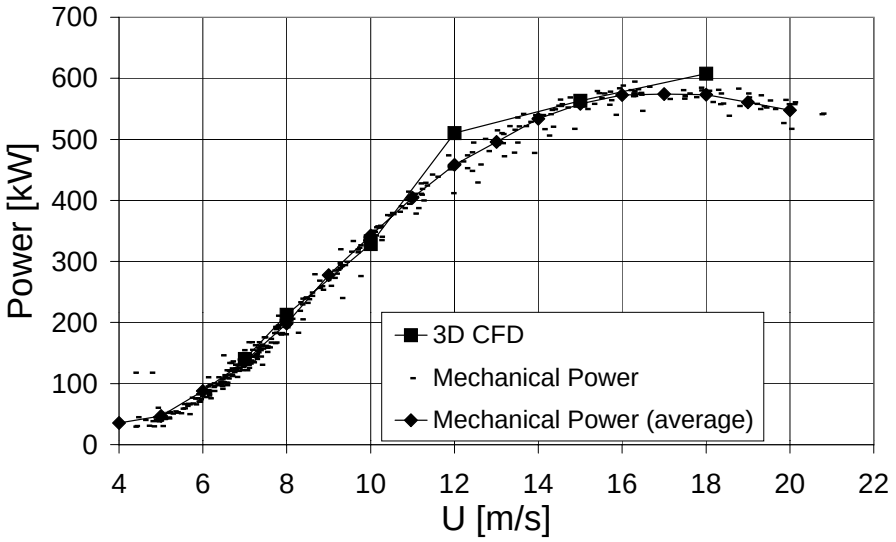

Figure 2-3 CFD computed power curve compared to measured power curve in form of 10-minute average and binned (Paulsen, 1995).

2.2 Methods for deriving data from 3D CFD

Momentum theory

Based on the 3D CFD force distributions for different wind speeds, the momentum theory was used. The momentum theory is a common way to calculate the force distribution on the blades in most computer codes for aerodynamics on wind turbines. It is based on airfoil characteristics. Since the force distribution was determined in the CFD calculations, the airfoil characteristics were determined in an inverse manner. For this purpose, the following equations described by, e.g., Andersen et al. (1980) were solved, where ϕ is the relative velocity angle to the rotor plan, a is the axial induction and a' is the tangential induction:

$$\tan(\phi) = \frac{1-a}{1+a'}\frac{V_0}{r\omega}, \qquad (2\text{-}7)$$

$$a = 1/(\frac{4\sin^2\phi}{\sigma C_y}F + 1), \qquad (2\text{-}8)$$

$$a' = 1/(\frac{4\sin\phi\cos\phi}{\sigma C_x}F - 1). \qquad (2\text{-}9)$$

V_0 is the wind speed, r is the local radius, ω is the rotational frequency and $\sigma=cB/(2\pi r)$ is the solidity, where c is the chord length and B is the number of blades. These quantities were all known. The coefficients, which was used, are defined by $C_x=F_x/(0.5\rho W^2 c)$ and $C_y=F_y/(0.5\rho W^2 c)$, where F_x and F_y are forces per meter in tangential and axial direction of the rotor plan, respectively. These forces were determined by the CFD calculations. $W=W(\phi)$ is the relative velocity on the airfoils, ρ is the density and F is the tip loss correction defined by $F=2\arccos(e^{-f})/\pi$, where $f=B(R-r)/(2r\sin\phi)$ and R is the rotor radius.

Since the model breaks down for $a > 0.5$ an empirical relation by Glauert described by Smith (1976) was used, which correct the axial induction, a:

$$\begin{aligned} a &= 1 - \sqrt{\frac{f_t}{F_t}} \\ f_t &= 1/\left[0.11(1/F_t)^3 - 0.70(1/F_t)^2 + 2.15(1/F_t) + 2.15\right] \\ F_t &= a/(1-a) \end{aligned} \qquad (2\text{-}10)$$

This correction was applied for low wind speeds, where the axial induction was big. The calculations were applied for several radii in spanwise direction. The result was a set of lift and drag coefficients, C_L and C_D, as a function of the angle of attack, α, for each radius, r. Lift and drag coefficients were calculated as $C_L=C_y\cos\phi+C_x\sin\phi$, $C_D=C_y\sin\phi-C_x\cos\phi$ and $\alpha=\phi-\theta$, where θ is the local twist.

Actuator disc theory

The second method, which was used to determine the airfoil characteristics, is based on the actuator disc model. The above described momentum theory is also based on the actuator disc concept. However, the main difference is that the full equations (the Navier-Stokes equations) describing the flow through an actuator disc are solved. In the momentum theory, simplified equations are used.

The actuator disc flow was solved using the general purpose CFD code FIDAP (1991) and application of this model to wind turbine rotor flow is presented by Madsen (1996). The axi-symmetric flow case was used and turbulent flow was modelled with a standard k-ε model. Inflow conditions were applied 6*R* upstream and outflow conditions were applied 5*R* in lateral direction and 40*R* downstream, Figure 2-4.

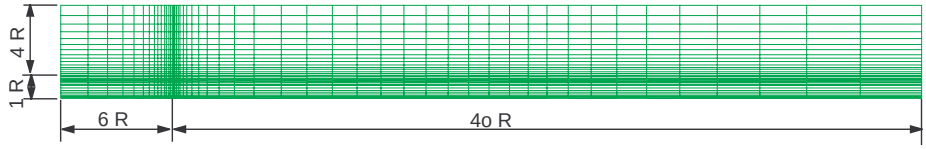

Figure 2-4 The mesh used for the actuator disc model flow has the dimensions: 6R upstream, 40R downstream and 5R in radial direction.

As in the above method using the momentum theory, the input for the calculations was the blade forces per unit blade length in axial and tangential direction, F_y and F_x, respectively. The volume forces f_n and f_t in axial and tangential direction, respectively, applied to the actuator disc were derived from the blade forces as follows:

$$f_n = \frac{BF_y}{2\pi r}\frac{1}{\Delta n}, \qquad (2\text{-}11)$$

$$f_t = \frac{BF_x}{2\pi r}\frac{1}{\Delta n}, \qquad (2\text{-}12)$$

where Δn is the thickness of the disc, which in the present calculations was set to a value of 0.05*R*.

With the applied volume forces on the actuator disc, the flow field was calculated and typical results are shown in Figure 2-5.

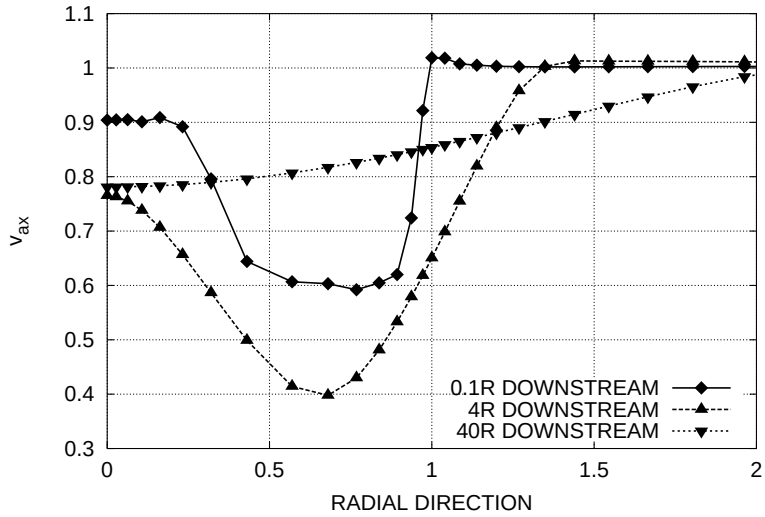

Figure 2-5 Computed axial velocity profiles at different downstream positions from the actuator disc. Applied loading for a free wind speed of 8 m/s.

On basis of the computed velocity at the rotor disc the angle of attack and the relative velocity to each blade segment could easily be computed using the geometrical relations for the blade and the operational parameters. Then C_L and C_D for each blade segment could be derived. It should be noted that in the actuator disc computations no tip correction method was applied. A comparison with the momentum theory data will be shown later.

Correction for measured power curve

Differences are observed when power curves from measurements and CFD calculations are compared, see Figure 2-3. These differences could be due to differences in the conditions. Thus, neither tower nor nacelle was modelled in the CFD calculations. Neither gusts were modelled. I.e., no dynamic phenomena were implied in the CFD calculations and steady state solutions were the result. In addition, uncertainties in the measurements and the quality of the turbulence model in the CFD calculations were factors that could influence the differences between the power curves.

To obtain airfoil characteristics from the CFD calculations that could reproduce the measured power the following procedure was followed:

- The power curve from the CFD calculations was scaled to the measured power curve. This produced a scaling factor for each wind speed.
- Axial and tangential force distributions from CFD calculations were linearly scaled with the corresponding scaling factors.
- Using the scaled force distributions, the airfoil characteristics were derived.

In this case, the greatest difference was found at 12 m/s, where the scaling factor had a value of 0.91.

Constructing airfoil characteristics

As shown in Figure 2-6 2D wind tunnel measurements were used at the linear part of the constructed C_L curve.

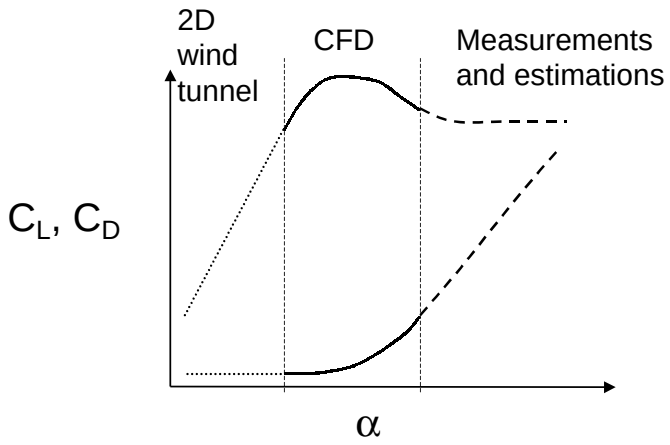

Figure 2-6 Sketch of the construction of airfoil characteristics.

At the linear part of the C_L curve, the 2D airfoil characteristics were believed to be more realistic than data from 3D CFD. In contrast, 2D airfoil characteristics in stall were believed to be unrealistic due to rotational effects and 3D effects. This is the reason for using airfoil characteristics in stall based on 3D CFD. Finally, measurements and estimations were used in deep stall. This was done because the 3D CFD computations were carried out for wind speeds below 18 m/s and because the 3D CFD computations were assumed steady state. The estimations were used since the flow in deep stall was fluctuating and strongly influenced by rotational effects and 3D effects.

2.3 Results

The description of the results is divided into three parts. The first part is a description of the airfoil characteristics derived directly from 3D CFD using momentum theory and actuator disc theory and compared to 2D wind tunnel measurements. The second part is a description of the airfoil characteristics derived from 3D CFD but corrected according to measurements. The third part is a description of aeroelastic computations in which the derived airfoil characteristics are used.

Airfoil characteristics direct from 3D CFD

C_L and C_D coefficients were derived applying the momentum theory and the actuator disc theory on the force distributions determined by the CFD calculations, see chapter 2.1. In Figure 2-7 to Figure 2-12 the coefficients in selected sections on the blade are compared to 2D wind tunnel measurements on NACA 63-4nn (Abbott and Doenhoff, 1959) and FFA-W3-nn1 (Fuglsang et al., 1998).

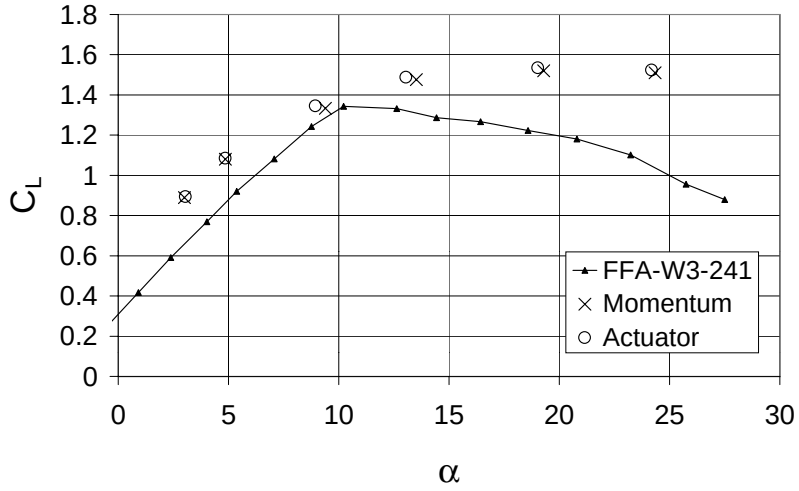

Figure 2-7 Derived C_L at r=10.0 m (t/c=24.19%) using momentum theory and actuator disc theory. Comparison with 2D wind tunnel measurements.

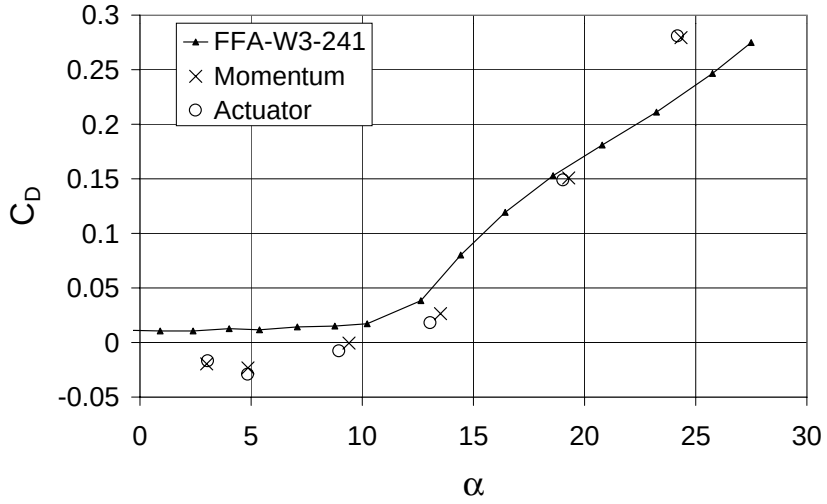

Figure 2-8 Derived C_D at r=10.0 m (t/c=24.19%) using momentum theory and actuator disc theory. Comparison with 2D wind tunnel measurements.

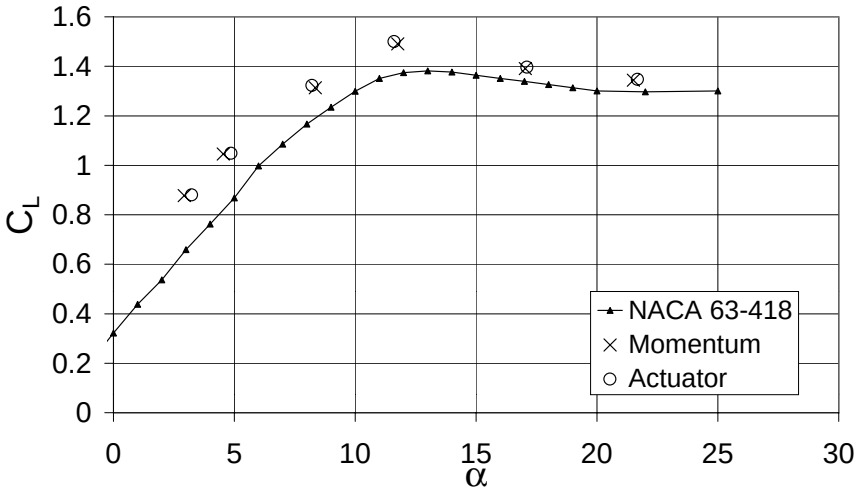

Figure 2-9 Derived C_L at r=12.5 m (t/c=18.20%) using momentum theory and actuator disc theory. Comparison with 2D wind tunnel measurements.

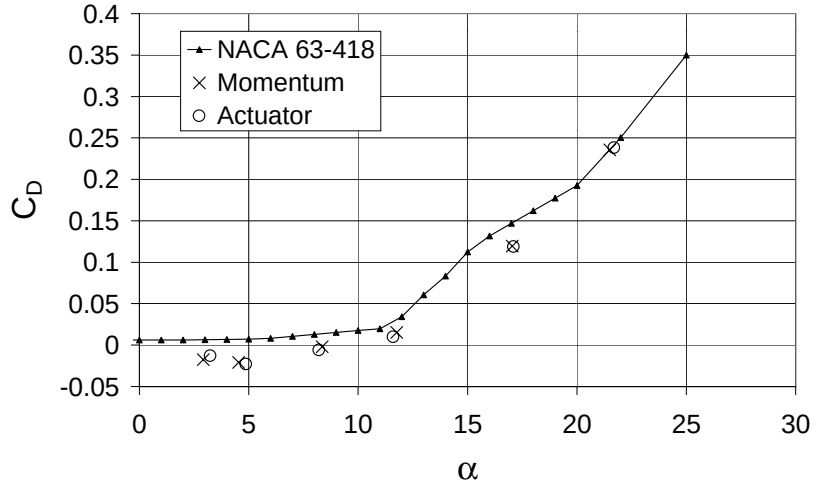

Figure 2-10 Derived C_D at r=12.5 m (t/c=18.20%) using momentum theory and actuator disc theory. Comparison with 2D wind tunnel measurements.

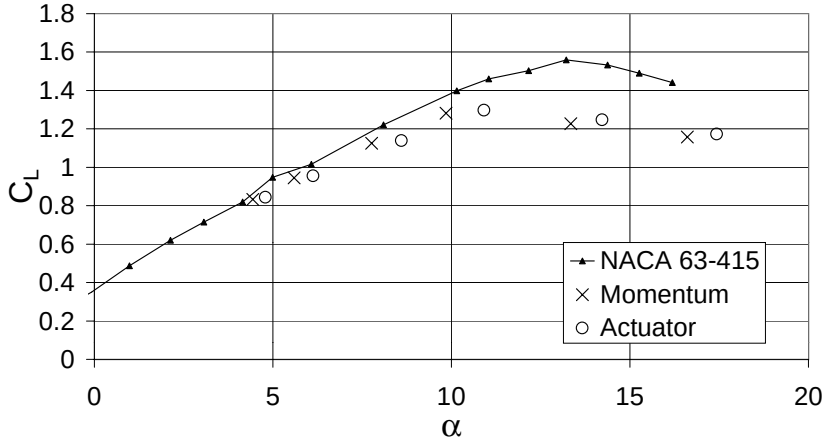

Figure 2-11 Derived C_L at r=19.0 m (t/c=15.75%) using momentum theory and actuator disc theory. Comparison with 2D wind tunnel measurements.

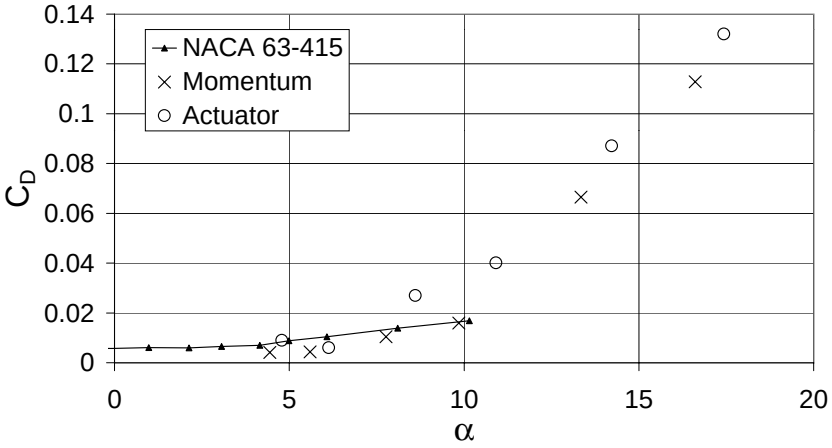

Figure 2-12 Derived C_D at r=19.0 m (t/c=15.75%) using momentum theory and actuator disc theory. Comparison with 2D wind tunnel measurements.

Comparing the derived airfoil coefficients obtained by momentum theory and actuator disc theory, only small differences were seen. The biggest difference was seen for C_D at the tip, r=19.0 m, where C_D derived using momentum theory was slightly lower than C_D derived using actuator disc theory.

Comparing the derived airfoil coefficients to 2D wind tunnel measurements, several differences were seen. For small angles of attack, C_L was too high and C_D was too low. In fact, C_D was negative for some angles of attack. This was probably due to an under-estimation of the axial induction in the CFD calculation. Furthermore, low C_L in stall was observed near the tip. Near the root high C_L were seen. At about 0.6R the airfoil characteristics were approximately the same.

Airfoil characteristics constructed on the basis of measurements and CFD

C_L and C_D coefficients were constructed using the method described in section 2.2. In Figure 2-13 to Figure 2-22 the coefficients are compared to 2D wind tunnel measurements on NACA 63-4nn (Abbott and Doenhoff, 1959) and FFA-W3-nn1 (Fuglsang et al., 1998). In the linear part of the C_L curve the above mentioned measurements were used. In stall, the airfoil characteristics derived from CFD and described above were used. Only small differences were seen between data derived using momentum theory and data derived using actuator disc theory. Thus, only data from momentum theory were used. In deep stall, the data were based partly on measurements (Bak and Petersen, 1998) and partly on estimations.

Two set of coefficients are shown:

- One set based on force distributions as computed directly in CFD. This set is called *Final Data*.
- Another set also based on force distributions as computed in CFD, but scaled in axial and tangential direction according to the measured power. This set is called *Final Data (corrected)*.

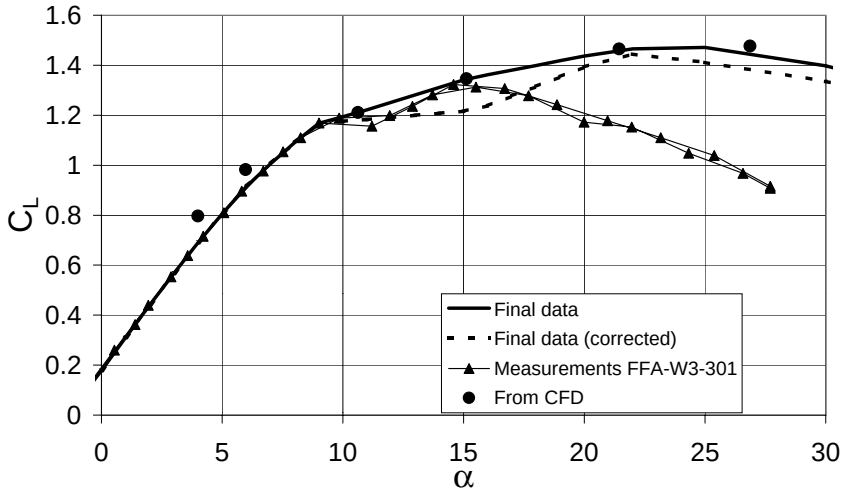

Figure 2-13 Constructed C_L at r=8.0 m corresponding to 33.06 % thickness. Comparison with 2D wind tunnel measurements.

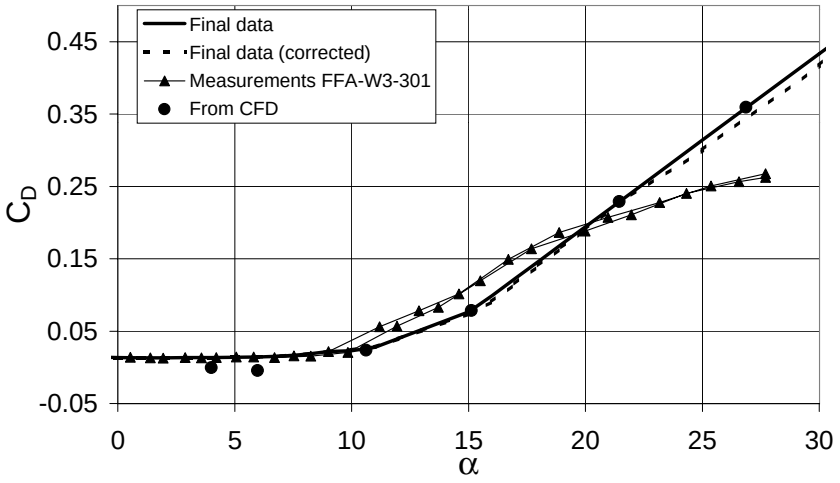

Figure 2-14 Constructed C_D at r=8.0 m corresponding to 33.06 % thickness. Comparison with 2D wind tunnel measurements.

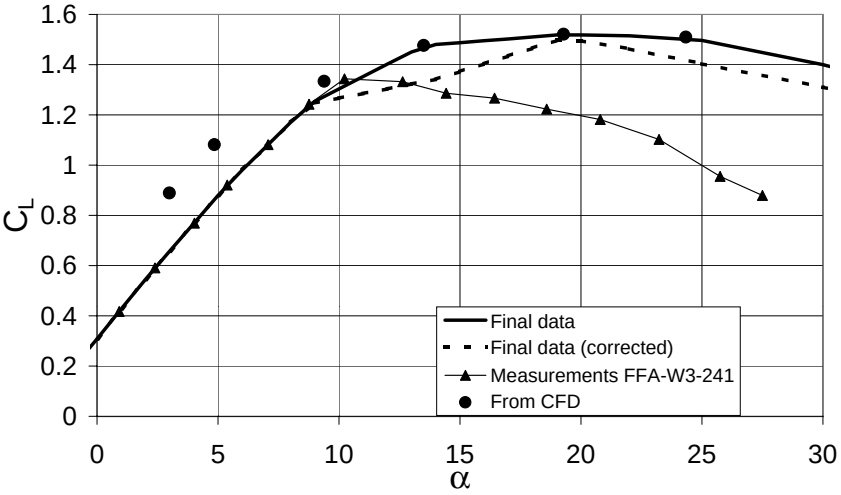

Figure 2-15 Constructed C_L at r=10.0 m corresponding to 24.19 % thickness. Comparison with 2D wind tunnel measurements.

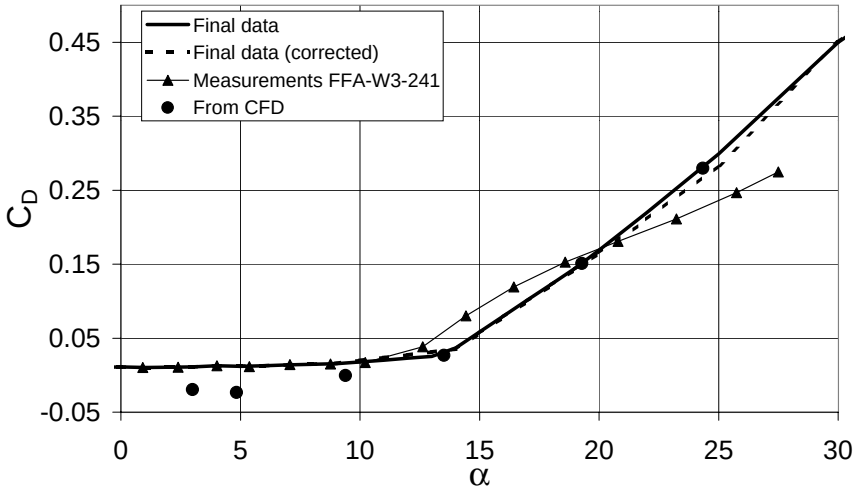

Figure 2-16 Constructed C_D at r=10.0 m corresponding to 24.19 % thickness. Comparison with 2D wind tunnel measurements.

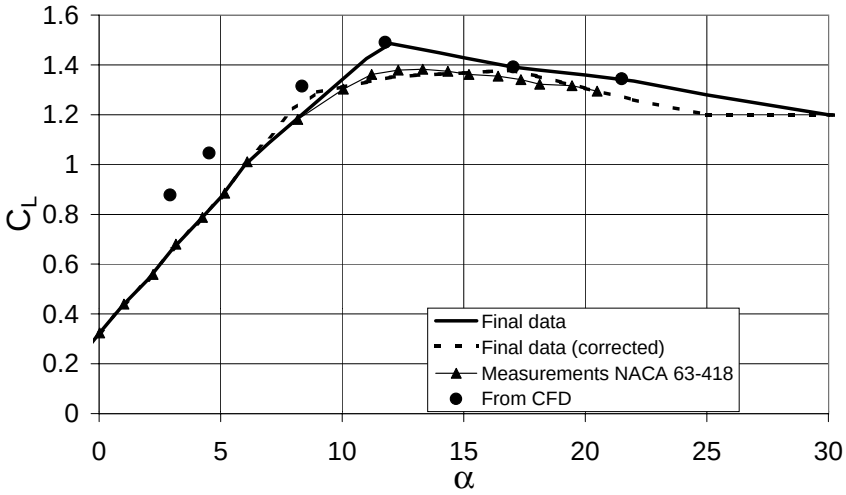

Figure 2-17 Constructed C_L at r=12.5 m corresponding to 18.20 % thickness. Comparison with 2D wind tunnel measurements.

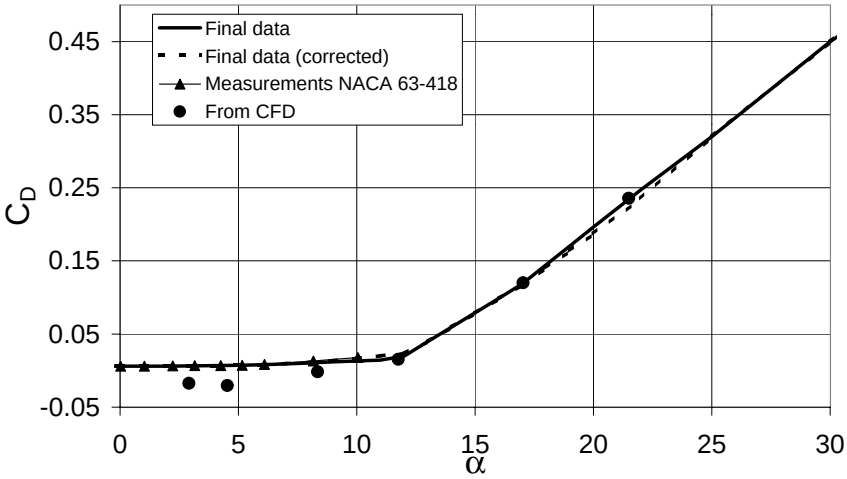

Figure 2-18 Constructed C_D at r=12.5 m corresponding to 18.20 % thickness. Comparison with 2D wind tunnel measurements.

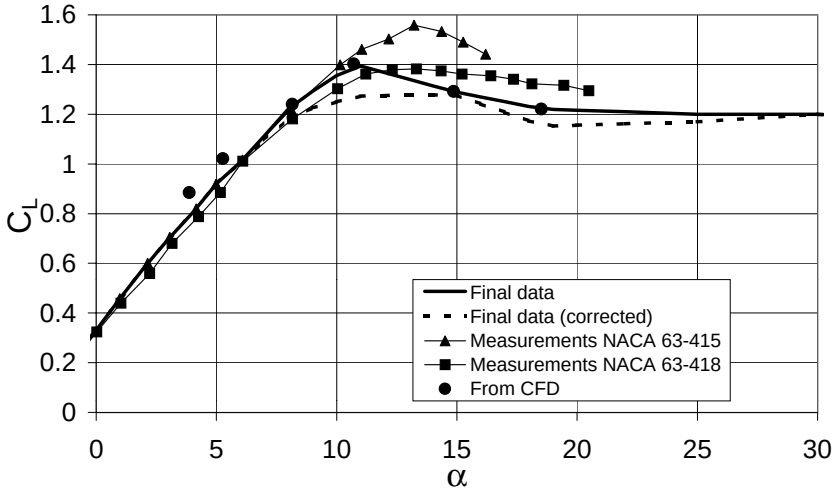

Figure 2-19 Constructed C_L at r=16.5 m corresponding to 16.55 % thickness. Comparison with 2D wind tunnel measurements.

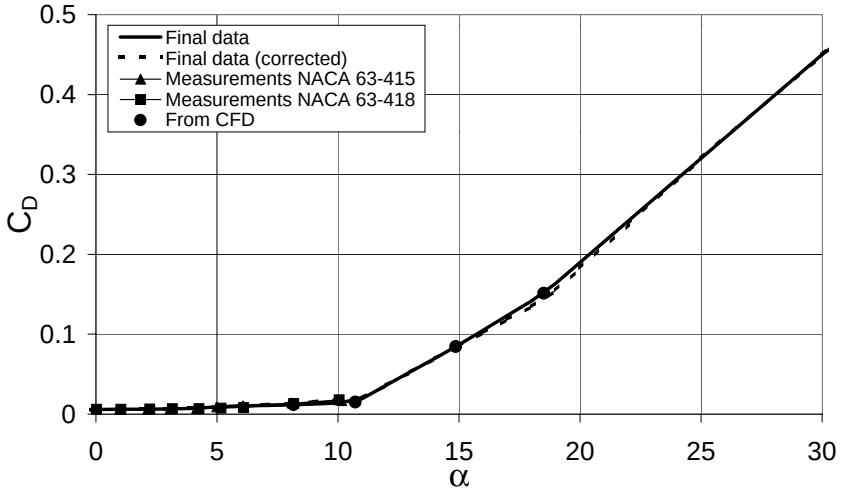

Figure 2-20 Constructed C_D at r=16.5 m corresponding to 16.55 % thickness. Comparison with 2D wind tunnel measurements.

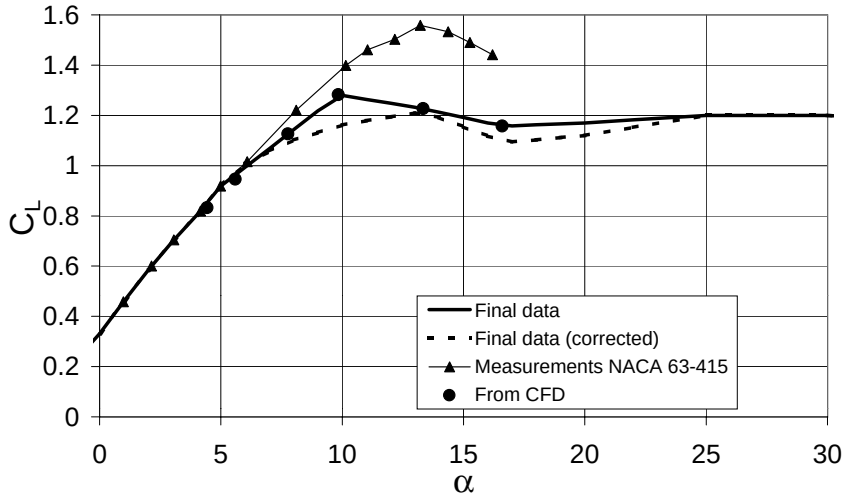

Figure 2-21 Constructed C_L at r=19.0 m corresponding to 15.75 % thickness. Comparison with 2D wind tunnel measurements.

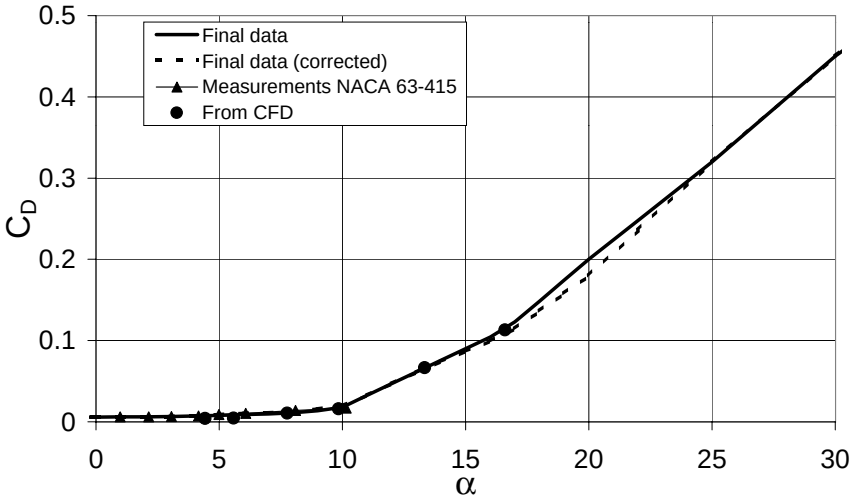

Figure 2-22 Constructed C_D at r=19.0 m corresponding to 15.75 % thickness. Comparison with 2D wind tunnel measurements.

At r=8.0 m and r=10.0 m C_L for both sets were higher in stall than for the wind tunnel measurements. However, the corrected set was in good agreement with the measurements at incipient stall, after which C_L increased. It should be noted that C_L increased until approximately α=20° in contrast to the measurements, where C_L decreased from α=10°. C_D were somewhat lower than the measurements until α=20° after which it increased.

At r=12.5 m the airfoil characteristics were in good agreement with measurements, however, with the uncorrected C_L somewhat higher.

At r=16.5 m and r=19.0 m C_L was low in stall compared to measurements, with the corrected data as the lowest. C_D was in good agreement with measurements until α=10°. For C_D no data was available for angles of attack greater than 10°.

Aeroelastic calculations with the derived airfoil characteristics

Using the constructed airfoil characteristics in aeroelastic computations five set were necessary to obtain the measured power curve (r=8.0 m, 10.0 m, 12.5 m, 16.5 m and 19.0 m). Very often only three sets are used in aerodynamic and aeroelastic computations. In this case it was important to state the exact relative thickness, e.g., t/c=16.55%, and to use three sets of airfoil characteristics on the outer part of the blade. This lead to force distributions, which reproduced both power and loads.

The aeroelastic calculations were carried out on a Nordtank NTK 500/41 using LM 19.1 blades with 1.5-m root extenders. The aeroelastic computer code was HawC (Petersen, 1996). The turbulence intensity was 10% for the wind speeds calculated: 8, 10, 12 and 16 m/s. For each wind speed five calculations were carried out with five different seed parameters, i.e., with five different turbulence histories. Each calculation determined the response for a 10-minutes period.

The calculations resulted in power and flap moments as shown Figure 2-23 to Figure 2-26. The computed power was averaged over the 10-minutes period. Compared to the measurements it was slightly over-predicted with the use of the uncorrected data. The computed flap moments using the corrected data were slightly under-predicted and slightly over predicted with the uncorrected data. It was noted that the effects from dynamics and averaging did not affect the calculation of power with the *Final Data (corrected)* since the calculated power predicted the measured power very well as it was expected. Using the *Final Data* it was expected that the CFD computed power curve would be predicted very well. However, the *Final Data* seemed to under-predict the power at 12 m/s and over-predict the power at 16 m/s. These deviations were due to an insufficient representation of the airfoil characteristics so that the force distribution for these wind speeds deviated from the original 3D CFD calculations. I.e., the deviation was due to neither dynamic effects nor averaging effects.

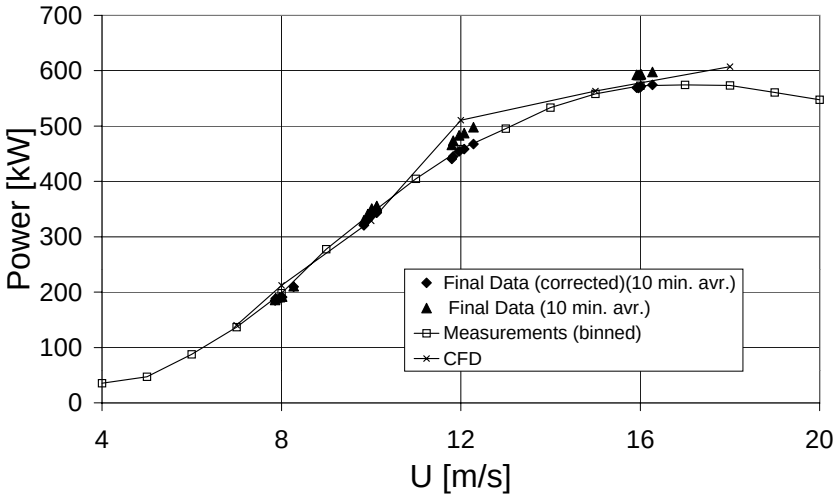

Figure 2-23 Calculated 10-minute average power based on 'Final Data' and 'Final Data (corrected)'. They are compared to power curves from measurements and CFD.

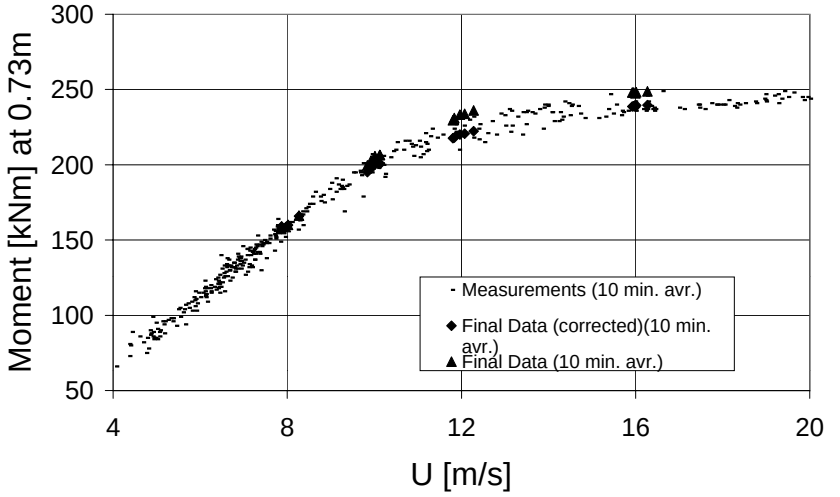

Figure 2-24 Computed flap moments in r=0.73 m, 0.04R, using 'Final Data' and 'Final Data (corrected)'. Comparison with measured flap moments.

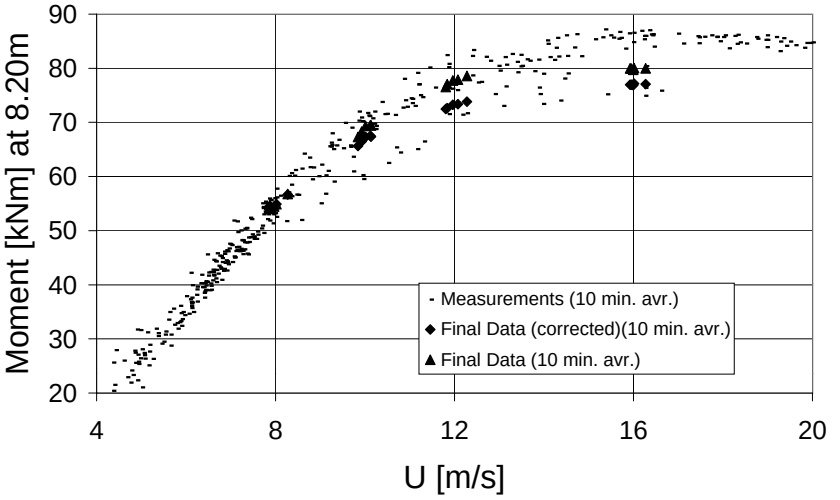

Figure 2-25 Computed flap moments in r=8.20 m, 0.40R, using 'Final Data' and 'Final Data (corrected)'. Comparison with measured flap moments.

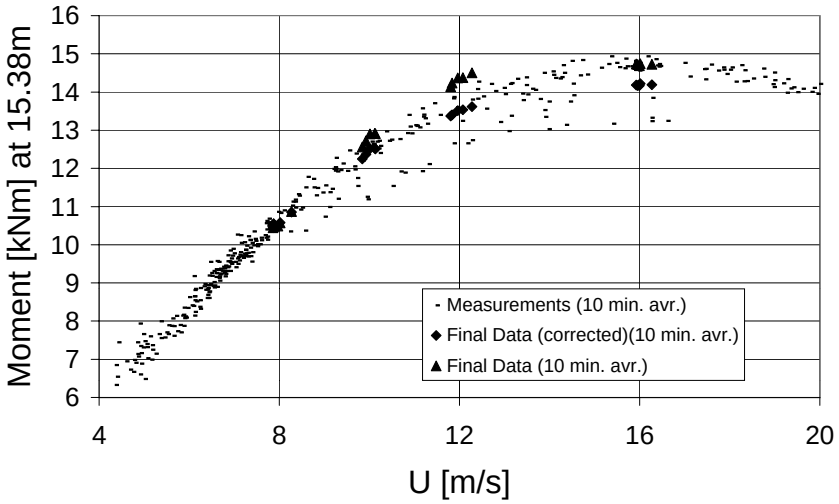

Figure 2-26 Computed flap moments in r=15.38 m, 0.75R, using 'Final Data' and 'Final Data (corrected)'. Comparison with measured flap moments.

Calculations on the same wind turbine operating in wind speeds from 6 to 24 m/s resulted in a fatigue analysis with equivalent loads as shown in Table 2-1. The turbulence intensity is given in Table 2-2. In Table 2-1 the loads calculated with the *Final Data (corrected)* are compared to loads calculated with *Original Data*. The *Original Data* were an example of a set among several sets used for this rotor and derived based on qualified estimations and experience. They are shown in Figure 2-27 to Figure 2-29 and compared to 2D wind tunnel measurements. The *Original Data* had a low C_L in stall at the tip (t/c=15%) and a high C_D in stall at the inner part of the rotor (t/c=21%) compared to the 2D measurements. For angles of attack beyond α=20° the data were based partly on measurements (Bak and Petersen, 1998) and partly on estimations.

Compared to the *Final Data (corrected)* the *Final Data* over-predicted all loads as expected. Comparing the *Original Data* to the *Final Data (corrected)* all loads were over-predicted from 1% to 15% except for the power. The agreement in power was because the *Original Data* were corrected so that the power corresponded to the measurements. The high C_L in stall caused the over-prediction of all other loads. It was higher at the tip and lower at the root compared to the *Final Data (corrected)*.

Table 2-1 Comparison of fatigue loads using different airfoil characteristics. The fatigue analysis is based on a stall regulated wind turbine with a 41-m rotor operating in wind speeds from 6 to 24 m/s. The number of load cycles is 10^7.

m	Load	Unit	Final Data (corrected) (1)	Final Data (2)	Fraction (2)/(1)	Original Data (3)	Fraction (3)/(1)
3	Power	kW	459.92	499.07	*1.09*	460.18	*1.00*
12	Flap moment (root)	kNm	233.61	239.35	*1.02*	243.70	*1.04*
12	Edge moment (root)	kNm	343.99	352.44	*1.02*	369.74	*1.07*
5	Tilt moment	kNm	326.23	358.19	*1.10*	347.37	*1.06*
5	Yaw moment	kNm	327.54	362.14	*1.11*	331.96	*1.01*
3	Tower moment L	kNm	1754.28	1950.18	*1.11*	1837.22	*1.05*
3	Tower moment T	kNm	645.86	786.08	*1.22*	741.52	*1.15*

Table 2-2 Turbulence intensity in the fatigue analysis.

U[m/s]	6	8	10	12	14	16	18	20	22	24
I[%]	18.3	17.8	17.2	16.6	16.0	15.4	15.0	14.8	14.6	14.5

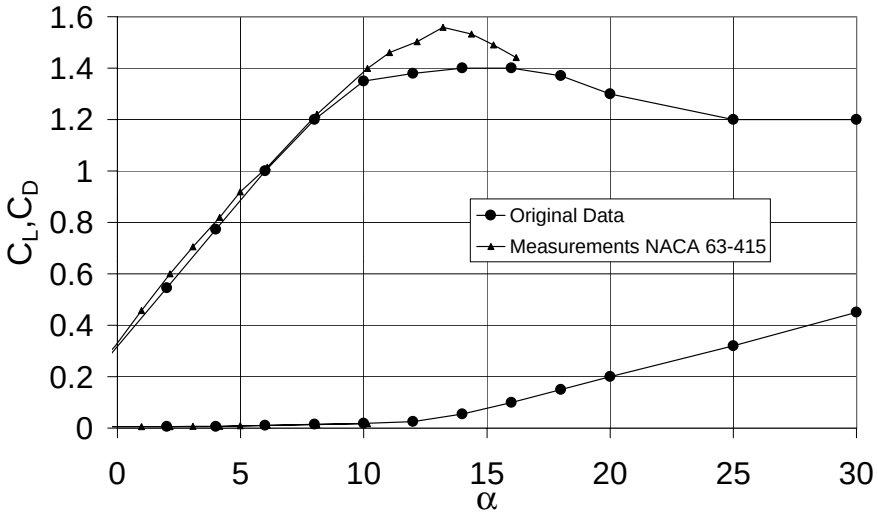

Figure 2-27 Original airfoil characteristics for t/c=15% on the LM 19.1 blade.

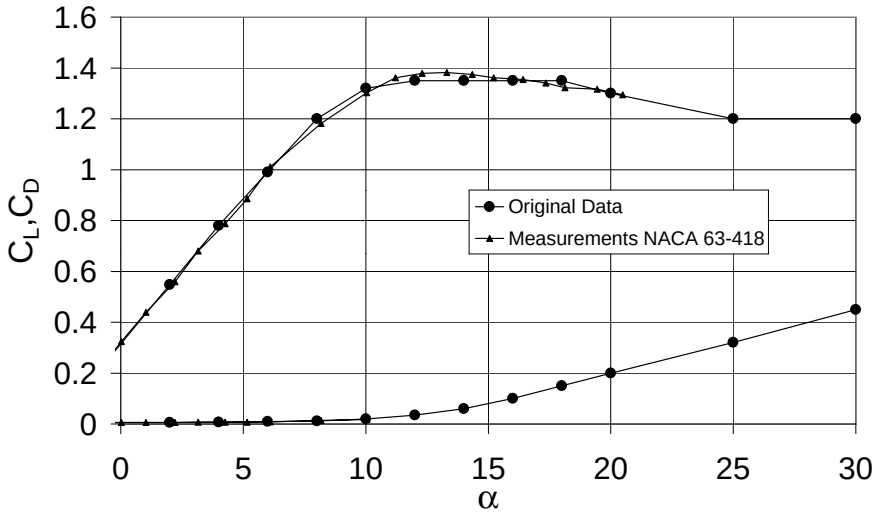

Figure 2-28 Original airfoil characteristics for t/c=18% on the LM 19.1 blade.

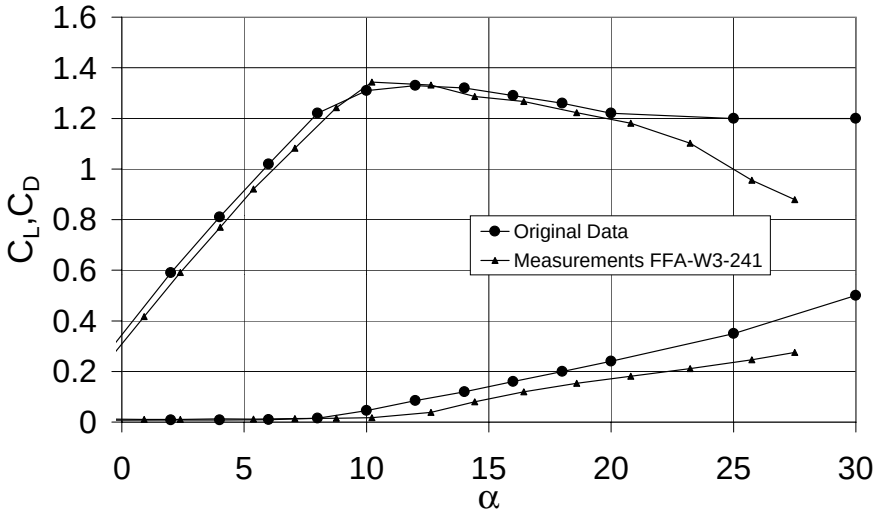

Figure 2-29 Original airfoil characteristics for t/c=21% on the LM 19.1 blade.

2.4 Conclusions

Airfoil characteristics for the LM 19.1 blade were constructed based on 2D wind tunnel measurements and CFD calculations on a full-scale 41-m rotor. The following conclusions are drawn:

- CFD computations on a full-scale rotor show promising results with deviation from measurements below 10 %,
- Airfoil characteristics derived by the inverse BEM method and the actuator disc method are in good agreement,
- Rotational and 3D effects are important,
- Compared to 2D wind tunnel measurements the results show that:
  - C_L is low in stall at the tip,
  - C_L is in good agreement at 0.6R,
  - C_L is high in stall at the inner part of the blade,
  - C_D is in good agreement at the outer part of the blade,
  - C_D is slightly lower at the inner part at the blade until α=20°, after which it increases,
- Aeroelastic computations using the constructed airfoil characteristics show good agreement with measured flap moments. Using the corrected data the moments are slightly under-estimated, while they are over-estimated using the uncorrected data,
- A fatigue analysis show that the use of corrected airfoil characteristics in calculations reduce the loads with up to 15% compared to commonly used airfoil characteristics,
- The aeroelastic computations reveal the importance of a sufficient resolution of the force distribution acting on the blades, i.e., a sufficiently number of sets of airfoil characteristics should be used on the blades.

3 Derivation by numerical optimisation

When Blade Element Momentum (BEM) theory is used to calculate power and loads, it is necessary to adjust the two-dimensional airfoil coefficients to achieve correct results. The adjustments compensate for the simplifications that form the basics for this relative simple theory such as the two-dimensional flow in annular stream tubes.

With some experience, it is possible to get good agreement between calculated and measured power by manually adjusting the airfoil C_L and C_D curves. There is in the literature guidelines of how the airfoil coefficients are affected by three-dimensional flow, Hansen and Øye (1998) and Bak and Petersen (1998). However, it is difficult at the same time to get agreement between measured and calculated loads. The power and in addition the blade bending moments are integral quantities, that do not in themselves contain information about the load distribution on the blades and therefore the determination of the correct blade force distribution is problematic.

To achieve the correct force distribution it is necessary to compare calculations of both power and multiple loads with measurements. This is a complex inverse problem, which can only be solved manually with difficulty. This chapter concerns a systematic method, where the airfoil coefficients are adjusted, so that there is agreement between measurements and calculations of power and loads. The method applies systematic numerical optimisation, where the error between measurements and calculations in terms of a least square sum is minimised by adjusting the airfoil coefficients in an iterative process.

3.1 Method for deriving data from measurements

The inverse problem of determining airfoil coefficients from measurements consists of the following parts:

1. Measurements of power and loads under normal operation.
2. An aeroelastic model of the blades and of the wind turbine structure in itself.
3. An aeroelastic code coupled to an optimisation algorithm.
4. An initial guess on the airfoil coefficients (C_L and C_D).

The measurements should cover normal operation in a large wind speed interval. To improve the statistical certainty, the measurements should be averaged into 10-minute values. Measurements at large yaw error or other non-typical operation conditions should be excluded. A mean value curve should be processed for each measured quantity by sorting the measurements into wind speed bins covering the wind speed operation interval.

An aeroelastic code should be used to calculate power and loads. This requires a valid aeroelastic model of the rotor, the nacelle and the tower. In this work, the FLEX4 code was used, Øye (1996). The calculations should be comparable to

the measurements. Therefore, the wind field was uniform without turbulence and the wind turbine structure had only few degrees of freedom. The necessary degrees of freedom depended on the measured loads. In case of blade-bending moments, flapwise and edgewise blade bending should be included and if tower bending moments are measured, tower bending should be included as well. The shaft rotation should of course always be included. In this way, quasi-steady calculations that include the centrifugal stiffening of the blades could be calculated as the time average of short time series.

The aeroelastic code should be coupled to an optimisation algorithm. In this work, the design tool, ROTOR was used, Fuglsang and Madsen (1999). The optimisation problem consists of the objective function, f, and the design variables in the design vector, $\boldsymbol{x}$. Furthermore the constraints, $\boldsymbol{g}$, can bound both design variables and calculated response parameters. The design variables are changed so that f is minimised.

The objective function, f, is calculated as a quadratic sum:

$$f = \sum_{i,j} \sqrt{\left(L_m - L_c\right)_{i,j}^2}, \qquad (3\text{-}1)$$

where L_m is a measured power or load and L_c is the corresponding calculated value, index i refers to the actual power/load and index j refers to the wind speed.

By minimising f the calculations will become closer to the measurements and eventually if f becomes zero, the calculations will be identical to the measurements at least at the wind speeds for which measurements and calculations are compared.

The design variables were the airfoil coefficients in terms of C_L and C_D as function of α. To limit the number of design variables and to ensure that the results were smooth curves, discrete co-ordinates determined interpolated curves for C_L and C_D. B-spline curves with $k = 5$, de Boer (1978), were used. The C_L and C_D curves were defined for different chord to thickness ratios corresponding to different blade positions, referring to the traditional definition of airfoil coefficients in BEM calculations.

An example of the parametric airfoil coefficients is shown in Figure 3-1. Six design variables described C_L and C_D, respectively. The design variables had fixed angles of attack but their value of C_L or C_D could be changed and this corresponded to a vertical movement in Figure 3-1.

There was in principle no guarantee for that the resulting C_L and C_D curves were physically obtainable. Possible errors could be non-linear C_L at low angles of attack or misalignment between maximum C_L and rise in C_D from separation. If only few powers/loads were compared to calculations or if the C_L and C_D curves did not contain a proper number of design variables, it was likely that the results would not be realistic. Too few design variables would cause too few degrees of freedom for the airfoil characteristics whereas too many design variables would cause too many possible solutions and most likely oscillations in the airfoil characteristics.

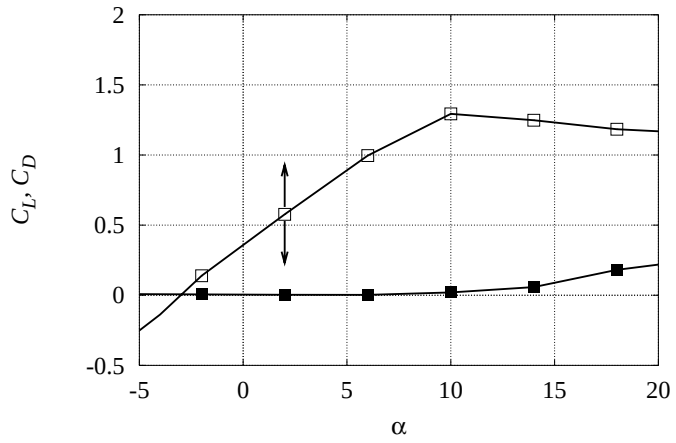

Figure 3-1 Parametric curves that describe C_L and C_D versus α. The discrete points are design variables.

3.2 Derivation from 3D CFD calculations

In this section airfoil coefficients are derived from the 3D CFD calculations of a full-scale rotor, which are described in section 2.1. The CFD calculations contained the blade force distributions; hence, a realistic test case could be constructed to validate the method. Furthermore, the results could be compared to the investigation in Section 2.3. Power and bending moment curves versus wind speed corresponding to measurements were constructed from the CFD calculations.

From the CFD calculations, the following measurements were derived:

- Mechanical power
- Blade root flapwise bending moment at r = 0.8 m.
- Blade bending moment around the chord axis at r = 8.0 m
- Blade bending moment around the chord axis at r = 10.0 m
- Blade bending moment around the chord axis at r = 12.5 m
- Blade bending moment around the chord axis at r = 16.5 m

The radii were chosen equal to those used in Section 2.3.

Airfoil sections were defined at the following blade radii corresponding to the LM 19.1 blade:

- *t/c* = 16.5% at *r* = 16.5 m corresponding to NACA 63-216.5,
- *t/c* = 18% at *r* = 12.5 m corresponding to NACA 63-418,
- *t/c* = 24% at *r* = 10 m corresponding to FFA-W3-241,
- *t/c* = 33% at *r* = 8 m corresponding to FFA-W3-331,

where *t/c* is the chord to thickness ratio and *r* is the blade radius.

In this case, the radii of the blade bending moments coincided with the airfoil sections. However, this is not required in the method.

For each airfoil, a model was used for which C_L and C_D versus α were two individual 6 point B-spline curves. The objective function was the quadratic sum of

the difference between power and loads at the wind speeds, 7, 8, 10, 12, 15 and 18 m/s corresponding to the calculated wind speeds.

Because the CFD calculations did not include centrifugal stiffening, the FLEX4 calculations were carried out with no degrees of freedom except for shaft rotation. The wind field was uniform without turbulence.

Results

The resulting airfoil coefficients can be seen in Figure 3-2 to Figure 3-5. The optimised airfoil coefficients are compared with 2D wind tunnel measurements referred to as *initial guess*.

Figure 3-2 shows the airfoil at t/c = 16.5% corresponding to NACA 63-416.5. The optimisation reduced maximum C_L. Minimum C_D at low angles of attack was also reduced whereas the rise in C_D from separation was increased. Both the reduction in maximum C_L and the rise in C_D around maximum C_L will limit the peak power.

Figure 3-3 shows the airfoil at t/c = 18% corresponding to NACA 63-418. Here, C_L at the entire operational range including maximum C_L was increased and C_D at separation was increased. The increase in the linear part of the C_L curve corresponds to a change in angle of attack at zero C_L toward negative.

Figure 3-4 shows the airfoil at t/c = 24% corresponding to FFA-W3-241. There was almost no change in C_L whereas the rise in C_D was moved to a lower angle of attack and the slope of C_D versus α was increased at high angles of attack.

Figure 3-5 shows the airfoil at t/c = 33% corresponding to FFA-W3-331. The optimised C_L was reduced around maximum C_L compared to 2D wind tunnel measurements and maximum C_L was moved to a higher angle of attack. The linear part of the C_L curve was very short indicating early separation. The minimum C_D was reduced but the rise in C_D at separation was not changed substantially.

For all airfoils, the rise in C_D from separation involved a steeper slope of C_D versus α and minimum C_D was reduced. At the outboard part of the blade, maximum C_L was reduced, whereas it was increased on the inboard part of the blade. This is in good agreement with the findings in Section 2.

The reduction in minimum C_D was a general tendency, this was somehow opposite of what could be expected, and it was not feasible. This could be caused by the nature of the smooth curves, where the bending of C_D at drag rise could not be modelled properly. To allow the steep rise C_D was reduced before drag rise. It could also be caused by uncertainties in the CFD calculations, in which minimum C_D might be under-estimated.

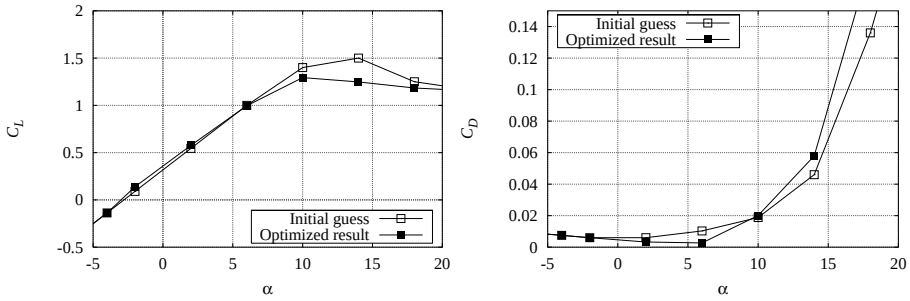

Figure 3-2 C_L and C_D at t/c = 16.5% at r = 16.5 m corresponding to NACA 63-216.5 for optimised result compared with initial guess.

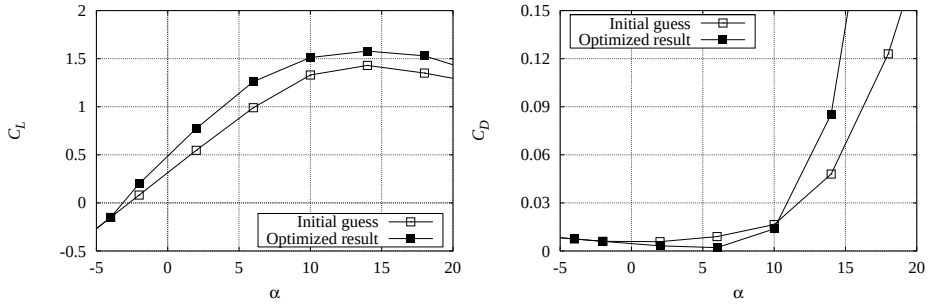

Figure 3-3 C_L and C_D at t/c = 18% at r = 12.5 m corresponding to NACA 63-418 for optimised result compared with initial guess.

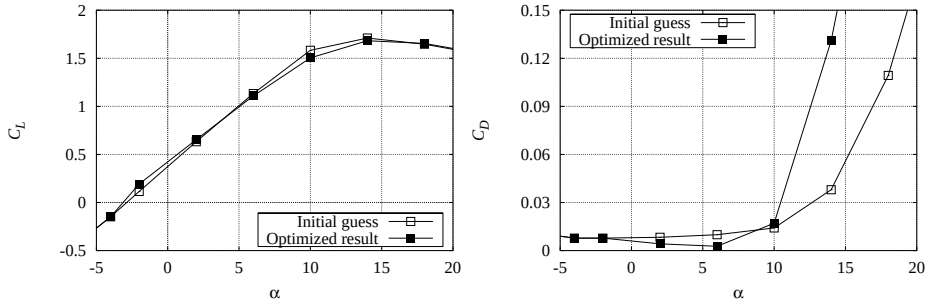

Figure 3-4 C_L and C_D at t/c = 24% at r = 10.0 m corresponding to FFA-W3-241 for optimised result compared with initial guess.

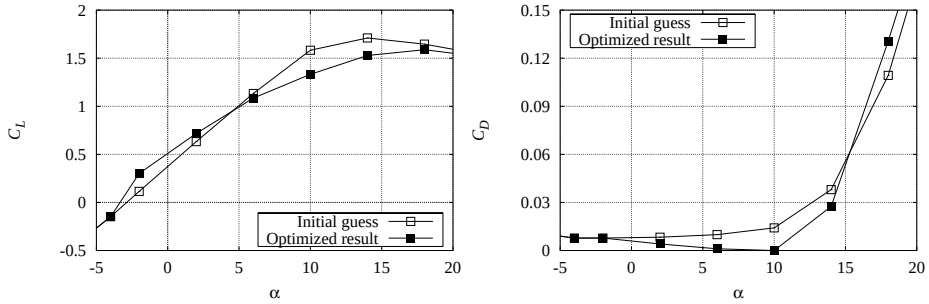

Figure 3-5 C_L and C_D at t/c = 33% at r = 8 m corresponding to FFA-W3-331 for optimised result compared with initial guess.

Figure 3-6 to Figure 3-9 show power and loads versus wind speed for the optimised airfoil coefficients compared to the target CFD calculation and to the curves from the initial guess on the airfoil coefficients. The initial guess was in

general different from the target CFD calculation and from the optimised results because the initial airfoil coefficients were based on 2D airfoil characteristics.

The mechanical power in Figure 3-6 for the optimised airfoil coefficients was in very good agreement with the target CFD calculation. However, there was a small discrepancy at low wind speeds and a small undershoot at 12 m/s. The rotor thrust force in Figure 3-7 was in good agreement with the target CFD calculation except for 18 m/s, for which the thrust from the optimised airfoil coefficients was too high. A high C_D caused this at high angles of attack. To limit the power and the loads at high wind speeds, the rise in C_D was increased and this resulted in too high C_D at 18 m/s and this was reflected on the thrust force.

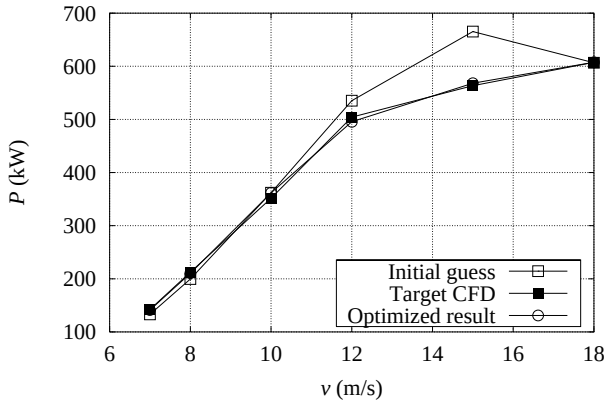

Figure 3-6 Mechanical power for optimised result compared with initial guess and target CFD.

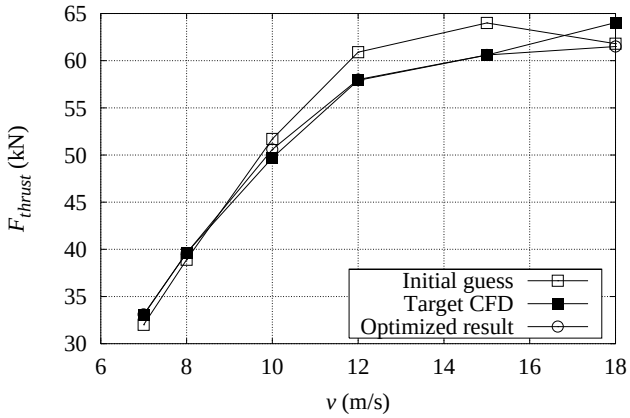

Figure 3-7 Rotor thrust force for optimised result compared with initial guess and target CFD.

Figure 3-8 and Figure 3-9 show the blade bending moments at r = 0.8 m and r = 12.5 m respectively. Except for the level of the bending moments, the curves look similar. The agreement between predicted values and the target CFD calculations was good except for 12 m/s.

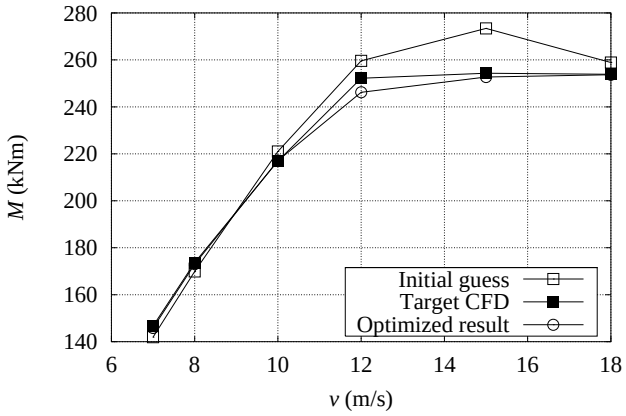

Figure 3-8 Blade root flapwise bending moment at r = 0.8 m for optimised result compared with initial guess and target CFD.

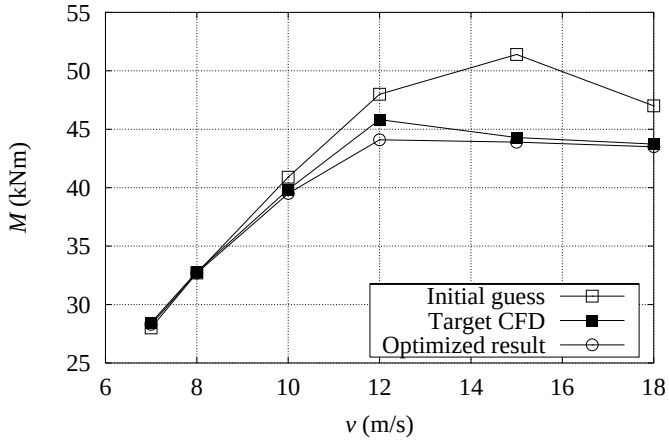

Figure 3-9 Blade bending moment around the chord axis at r = 12.5 m for optimised result compared with initial guess and target CFD.

In general, the agreement between the response from the optimised airfoil characteristics and the target CFD calculations was very good. It was a common tendency, that the response was predicted too low at 12 m/s. This is caused by the smooth curves for C_L and C_D, which do not allow a sharp edge at stall so that the power and the load curves become too smooth at 12 m/s. Apparently, use of the derived airfoil characteristics will result in good results for the power and for the analysed loads.

The results showed that the method could provide feasible airfoil characteristics that made it possible to calculate power and loads by use of BEM theory. There were only small deviation between the predicted power and loads and the target CFD calculations.

3.3 Derivation from measurements

In this section airfoil coefficients will be described, which were derived from the measurements on a Nordtank NTK 41 with a rotor with LM 19.0 blades with no aerodynamic devices, i.e., no stall strips, vortex generators etc. Petersen and Madsen (1999) performed the measurements.

The measurements were reduced to mean values versus wind speed. The original set of 10-minute values was reduced so that only normal operation measurements were present. After that, the 10-minute values were sorted in wind speed bins of width 1 m/s. The wind speed range extended from 5 m/s to 18 m/s. High wind speed measurements were not available.

In the investigation, the following measurements were used:

- Electrical power
- Blade root flapwise bending moment at r = 0.8 m.
- Blade bending moment around the chord axis at r = 5.1 m
- Blade bending moment around the chord axis at r = 10.3 m
- Blade bending moment around the chord axis at r = 15.3 m

Airfoil sections were defined at the following blade radii corresponding to the LM 19.0 blade:

- t/c = 15% at r = 20.5 m corresponding to LM2-15
- t/c = 18% at r = 13.9 m corresponding to LM2-18
- t/c = 21% at r = 12.2 m corresponding to FFA-W3-211
- t/c = 30% at r = 10.0 m corresponding to FFA-W3-301

For each airfoil a 6 point B-spline curve was used for C_L and C_D as in Section 3.2. The objective function was the quadratic sum of the difference between measured power and loads at the wind speeds, 7, 8, 10, 12, 14 and 16 m/s.

The FLEX4 calculations were carried out with an aeroelastic model of the wind turbine. The wind field was uniform without turbulence and the wind turbine structure had only few degrees of freedom for the blades and for shaft rotation. In this way, a quasi-stationary value for power and loads could be calculated that included the centrifugal stiffening of the blades.

Raw data and mean loads

Figure 3-10 and Figure 3-11 show the measured electrical power and the blade root flapwise bending moment respectively. The wind speed range was between 5 m/s and 18 m/s and each symbol is a 10-minute average value. The mean value curves that were used as target curves are also shown.

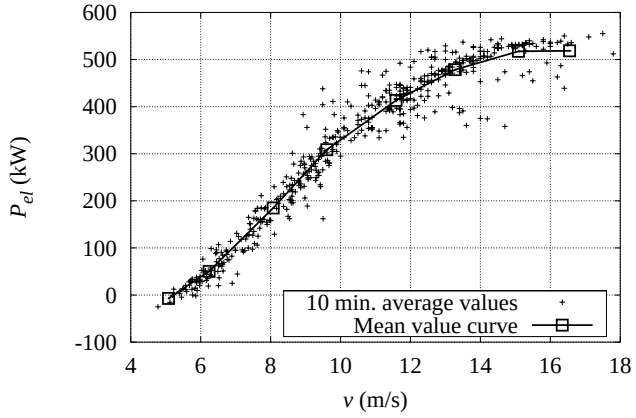

Figure 3-10 Measured electric power 10-minute average values and average value curve.

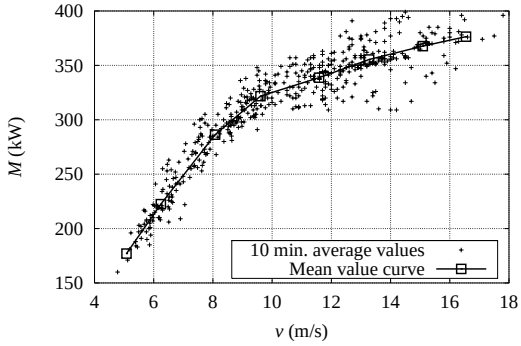

Figure 3-11 Measured blade root flapwise bending moment 10-minute average values and average value curve.

Results

The resulting airfoil coefficients can be seen in Figure 3-12 to Figure 3-15 in which the optimised airfoil coefficients are compared to 2D wind tunnel measurements.

Figure 3-12 shows C_L and C_D for the LM2-15 airfoil and the optimised airfoil coefficients at t/c = 15%. There was in general good agreement for C_L. Maximum C_L and the post stall area was equal but the slope of the linear part of the C_L curve at low α was changed so that the slope was steeper for the optimised result. For the C_D curve, the optimisation had increased C_D at high angles of attack. This would reduce the power at high wind speeds.

Figure 3-13 shows C_L and C_D for the LM2-18 airfoil compared to the optimised airfoil at t/c = 18%. The optimised airfoil coefficients were similar to the optimised airfoil coefficients at t/c = 15%. There were only minor differences in C_L. For the C_D curve, C_D at low angles of attack was reduced compared to LM2-18 and the drag rise was moved to a lower angle of attack resulting in earlier separation.

Figure 3-14 and Figure 3-15 show C_L and C_D for the FFA-W3-211 and FFA-W3-301 airfoils respectively. Whereas C_L was nearly unchanged, the C_D curve was changed so that the drag rise appeared at a lower angle of attack.

In general, the C_L curves for the optimised airfoil coefficients were not significantly changed but the C_D curves were changed so that the drag rise related to separation occurred at a lower angle of attack. That implied earlier separation compared to the 2D airfoil characteristics.

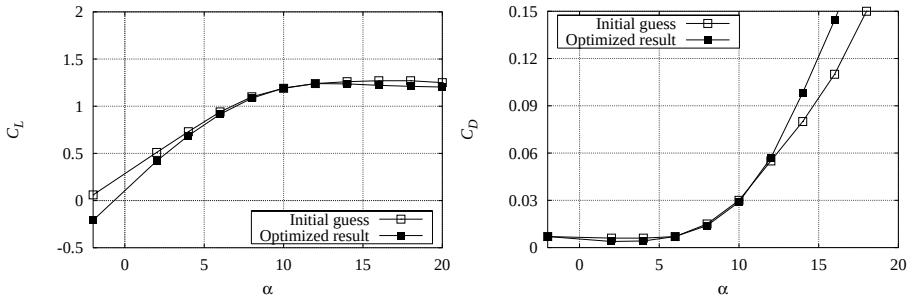

Figure 3-12 C_L and C_D at t/c = 15% at r = 20.5 m corresponding to LM2-15 for optimised result compared with initial guess.

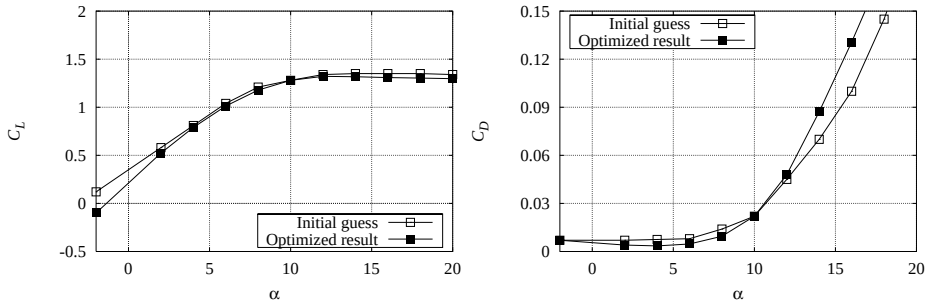

Figure 3-13 C_L and C_D at t/c = 18% at r = 13.9 m corresponding to LM2-18 for optimised result compared with initial guess.

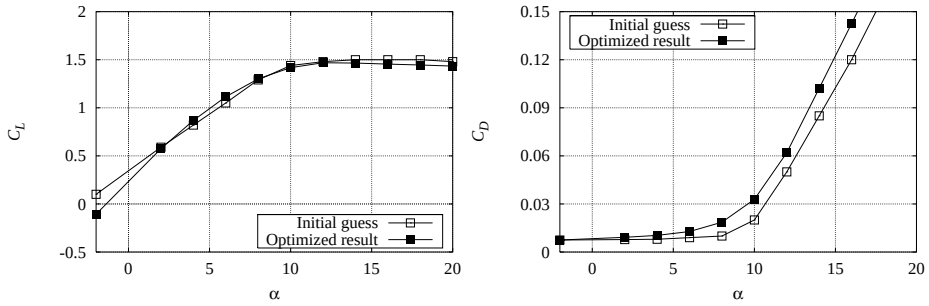

Figure 3-14 C_L and C_D at t/c = 21% at r = 12.2 m corresponding to FFA-W3-211 for optimised result compared with initial guess.

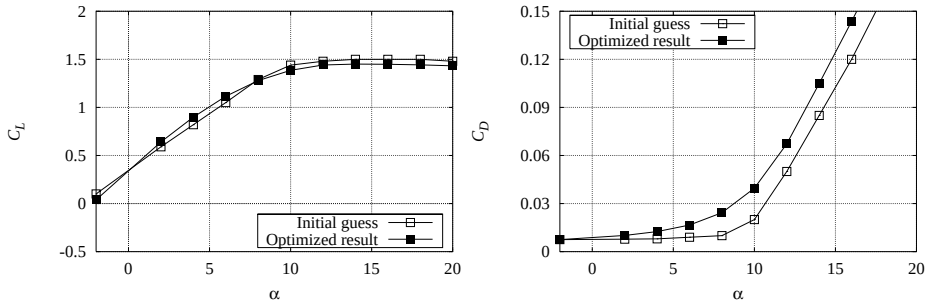

Figure 3-15 C_L and C_D at t/c = 30% at r = 10 m corresponding to FFA-W3-301 for optimised result compared with initial guess.

Figure 3-16 to Figure 3-18 show power and loads versus wind speed for the optimised airfoil coefficients compared to the target measurements and compared to power and loads resulting from the initial guesses on airfoil coefficients.

Figure 3-16 shows the electrical power curves. The power curve from the optimised airfoil coefficients was in good agreement with the measurement target except for around 12 m/s, where the power was too low. This was also the case for the CFD calculations, section 3.2.

Figure 3-17 shows the blade root flapwise bending moment at r = 0.8 m and Figure 3-18 shows the blade bending moment around the chord axis at r = 10.3 m. The agreement between calculated bending moments from the optimised airfoil coefficients and the target measurement was not as good as it was the case for the electrical power. The slopes of the curves were too low at low wind speeds and too high at high wind speeds. This could be caused by an offset

problem for the target measurements. Uncertainties in the calibration of the different moments could cause a misalignment between power and moments.

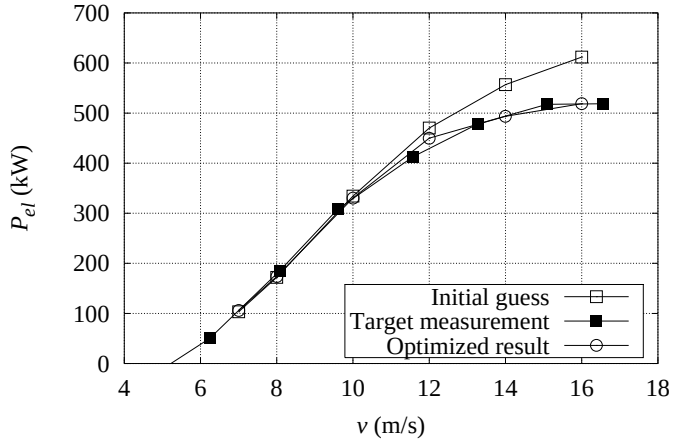

Figure 3-16 Electric power for optimised result compared with initial guess and target measurements.

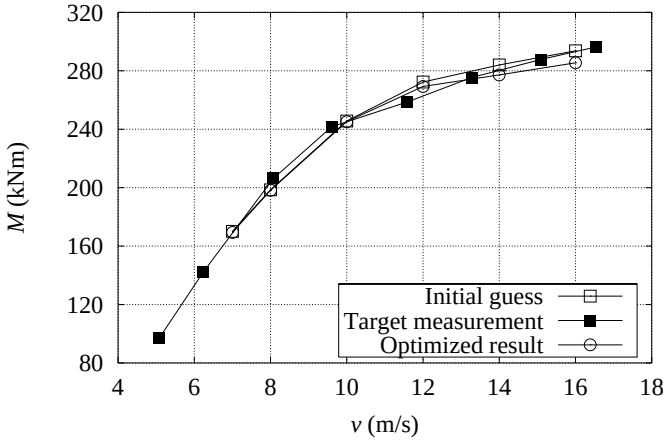

Figure 3-17 Blade root flapwise bending moment at r = 0.8 m for optimised result compared with initial guess and target measurements.

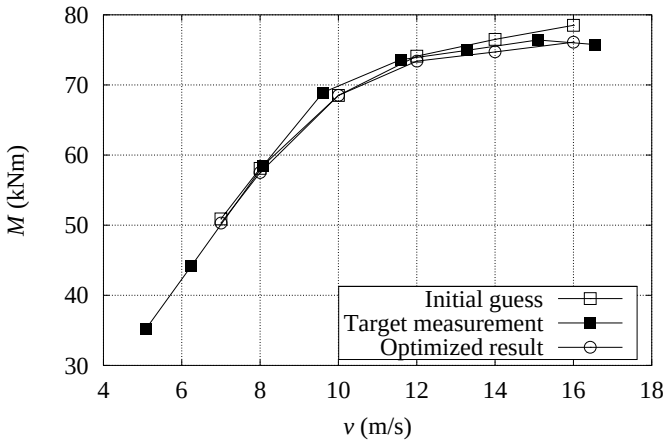

Figure 3-18 Blade bending moment around the chord axis at r = 10.3 m for optimised result compared with initial guess and target measurements.

3.4 Conclusions

In this chapter, we carried out adjustments of the airfoil coefficients, C_L and C_D to CFD calculations and measurements of power and loads by use of numerical optimisation. The results were promising since we succeeded to derive a set of C_L and C_D curves that could be used to calculate mean values of power and loads. In particular the power curves were well calculated by use of the optimised airfoil characteristics.

It was a general problem in the method, that the measured information that was used was integral values such as power and moments. These values did not contain sufficient information about the force distributions on the blades to an unambiguous determination of C_L and C_D. The calibration of measurements was a problem. Furthermore, it was difficult to find reliable measurements of loads, which provided information about the main flow direction perpendicular to the plane of rotation.

Although the methods involve multiple sources of uncertainty, reliable C_L and C_D curves can be derived if the following points are taken into account:

- As a minimum, the method should be used with measurements of power and blade root flapwise bending moment in a wind speed interval, which is as large as possible.
- It will be an advantage also to have measurements of other loads such as bending moments on tower and blade root bending moment in the edgewise direction. This was however not possible in this investigation.
- Only high quality measurements should be used and the statistical certainty should be as high as possible by using average values of many time series.
- Possible problems with calibration of measurements should be avoided by adjusting the mean level of the measurements to the calculated loads in the linear part of the C_L range based on two-dimensional C_L data.
- The C_L and C_D curves should be described with a sufficient number of design variables to resolve abrupt changes in slope, such as at maximum C_L, but without introducing oscillations in the resulting curves.

Future work with the method should involve a more comprehensive investigation of what measured loads that are necessary for correct derivation of C_L and C_D and a sensitivity study of the results.

4 Derivation by quasi-3D CFD computations

Compared to wind tunnel measurements and airfoil computations the characteristics for airfoil sections on wind turbine blades are influenced by rotation and 3D flow. Since 2D computations give a fast way to obtain the characteristics, it is desirable to take account for rotational and 3D effects in computations on airfoil sections described in 2D airfoil computations. Earlier works on this subject have been carried out by, e.g., Sørensen and Sørensen (1995).

In the following, a quasi-3D CFD model is presented. In the proposed model, the full Navier-Stokes equations are approximated using an order of magnitude analysis on the spanwise derivatives. This results in a quasi-3D formulation in which rotational effects and radial flow components are maintained. Therefore, the calculation needs only to be carried out on a 2D airfoil; hence reducing the computing costs in the order of what is typical for a pure 2D calculation. Earlier, similar approaches have been made in fixed-wing aerodynamics by applying the infinite-swept-wing approximation on the boundary layer equations, see, e.g., Cebeci (1974) and Radwan and Lekoudis (1984). For a rotating blade, such an approximation has been implemented and used in viscous/inviscid coupling algorithms by Snel et al. (1993) and Sørensen (1986). However, this is the first time it has been applied on the unsteady Navier-Stokes equations in a rotating frame of reference.

4.1 Method

Consider a blade section performing a rotating motion. Let *(oxyz)* be the rotating reference system associated with constant angular velocity Ω_y and let *oz* define the spanwise direction of the blade. Define by $\vec{u} = (u, v, w)$ the velocity and by $\vec{\omega} = (\omega_x, \omega_y, \omega_z)$ the vorticity in the rotating reference system.

Hypotheses

By considering the flow around an infinite cylinder of arbitrary cross-section rotating steadily about the (negative) *y*-axis (see Figure 4-1) it is shown by Sears (1950) that the inviscid velocity components may be written as

$$u = \Omega_y z \frac{\partial \phi}{\partial x}, \qquad (4\text{-}1)$$

$$v = \Omega_y z \frac{\partial \phi}{\partial y}, \qquad (4\text{-}2)$$

$$w = \Omega_y \left[2x - \phi\right], \qquad (4\text{-}3)$$

where $\phi = \phi(x,y)$ denotes the equivalent 2D velocity potential due to a blade translated with unit speed in the negative *x*-direction.

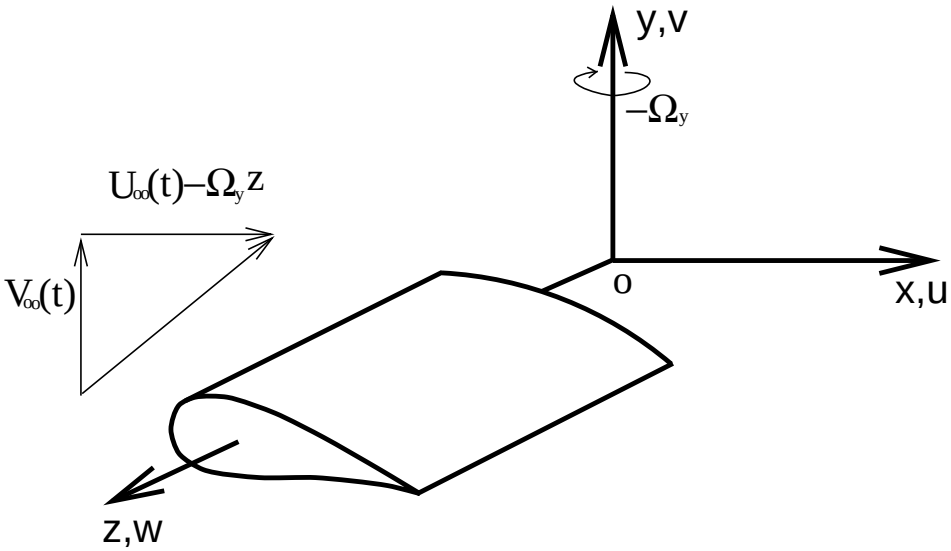

Figure 4-1 Definition of the coordinates.

It is readily seen that the velocity components, *u* and *v*, are given in a form as would be expected for a simple 2D analysis. It is not obvious, however, that the spanwise velocity component can be expressed in a simple formula, which depends only on the velocity potential of the equivalent 2D flow.

In a later analysis of Fogarty and Sears (1950) it is shown that the expression for the spanwise velocity component is the same even if the blade is advancing in the direction perpendicular to the plane of rotation, i.e., the *y*-direction. To derive an extended 2D approach in which the important effects of Coriolis and centrifugal forces are included we sought a plausible approximation that allowed us to get rid of the spanwise derivatives in the 3D equations. An approximation that was consistent with eqs. *(4-1)-(4-3)* was to assume the following similarity expressions for the velocity components

$$u = f(x, y)z, \tag{4-4}$$

$$v = g(x, y)z, \tag{4-5}$$

$$w = h(x, y). \tag{4-6}$$

These expressions then lead to the basic hypothesis

$$\frac{\partial u}{\partial z} = \frac{u}{z}, \tag{4-7}$$

$$\frac{\partial v}{\partial z} = \frac{v}{z}, \tag{4-8}$$

$$\frac{\partial w}{\partial z} = 0, \tag{4-9}$$

In the boundary layer, eqs. *(4-4)-(4-6)* assume similarity with a scaling of the spanwise distance, *z*, for the chordwise velocity components. The spanwise velocity distribution was assumed the same at all spanwise positions. This obviously introduced deviations, as compared to a full 3D representation, which were difficult to quantify completely. However, an order of magnitude analysis of the terms that were modified or neglected in the full 3D equations was performed. From this it was found that in the worst case the error would be of $O(c/z)^2$ for attached flow and of $O(c/z)^{2/3}$ in the case of separation. It should be noted, however, that the aim of the quasi-3D model was to enrich a 2D airfoil code with effects from the influence of Coriolis and centrifugal forces. Thus, employing eqs. *(4-7)-(4-9)* to neglect terms containing *z*-derivatives a set of equations may be derived that is much simpler than the full 3D equations and which contains 3D terms to leading order in *c/z* for both attached and separated flows.

Formulation

The motion of a viscous incompressible flow in a rotating reference system is governed by the time-averaged Navier-Stokes equations. In these equations the Reynolds stresses were modelled by introducing an eddy viscosity ν_t,

$$-\overline{u_i' u_j'} = \nu_t \left(\frac{\partial u_i}{\partial x_j} + \frac{\partial u_j}{\partial x_i}\right), \qquad (4\text{-}10)$$

where u_i' denotes a fluctuating velocity component and $\overline{()}$ is the time averaging. For simplicity we assumed

$$\frac{\partial \nu_t}{\partial z} = 0. \qquad (4\text{-}11)$$

Using the eq. *(4-7)*, we got

$$\frac{\partial^2 u}{\partial z^2} = \frac{\partial}{\partial z}\left(\frac{\partial u}{\partial z}\right) = \frac{\partial}{\partial z}\left(\frac{u}{z}\right) = \frac{z\partial u/\partial z - u}{z^2} = \frac{zu/z - u}{z^2} = 0.$$

Using the eqs. *(4-8)* and *(4-9)*, similar expressions were obtained for the other velocity components

$$\frac{\partial^2 v}{\partial z^2} = 0,$$
$$\frac{\partial^2 w}{\partial z^2} = 0.$$

Consequently, the *z*-derivatives of the diffusion terms in the time-averaged Navier-Stokes equations vanished.

We then considered the vorticity definition. The quasi-3D vorticity definition is given as

$$\omega_x = \frac{\partial w}{\partial y} - \frac{v}{z}, \qquad (4\text{-}12)$$

$$\omega_y = \frac{u}{z} - \frac{\partial w}{\partial x}, \qquad (4\text{-}13)$$

$$\omega_z = \frac{\partial v}{\partial x} - \frac{\partial u}{\partial y}. \qquad (4\text{-}14)$$

In the time-averaged Navier-Stokes equations, the only z-derivative left was the pressure. But there is no hypothesis, neither for the static pressure, p, nor for the total pressure, P. To overcome this difficulty, we considered the curl operator defined above, $(\partial/\partial x, \partial/\partial y, 1/z)\times$, and kept in mind that the curl of a gradient operator is zero. Then the only possible hypothesis for the pressure was that

$$\frac{\partial(p+|\vec{u}|^2/2+(\vec{\Omega}\cdot\vec{r})^2/2-\Omega^2 r^2/2)}{\partial z} = \frac{(p+|\vec{u}|^2/2+(\vec{\Omega}\cdot\vec{r})^2/2-\Omega^2 r^2/2)}{z}. \qquad (4\text{-}15)$$

From eq. *(4-9)* and the law of continuity the divergence of the velocity became

$$\frac{\partial u}{\partial x} + \frac{\partial v}{\partial y} = 0.$$

Then the quasi-3D formulation in velocity-pressure variables read

$$\frac{\partial u}{\partial t} + w\omega_y - v\omega_z + 2w\Omega_y = -\frac{\partial P}{\partial x} + 2\frac{\partial}{\partial x}(\nu^* \frac{\partial u}{\partial x}) + \frac{\partial}{\partial y}\left[\nu^*(\frac{\partial u}{\partial y} + \frac{\partial v}{\partial x})\right], \qquad (4\text{-}16)$$

$$\frac{\partial v}{\partial t} + u\omega_z - w\omega_x = -\frac{\partial P}{\partial y} + \frac{\partial}{\partial x}\left[\nu^*(\frac{\partial u}{\partial y} + \frac{\partial v}{\partial x})\right] + 2\frac{\partial}{\partial y}(\nu^* \frac{\partial v}{\partial y}), \qquad (4\text{-}17)$$

$$\frac{\partial w}{\partial t} + v\omega_x - u\omega_y - 2u\Omega_y = -\frac{P}{z} + \frac{\partial}{\partial x}(\nu^* \frac{\partial w}{\partial x}) + \frac{\partial}{\partial y}(\nu^* \frac{\partial w}{\partial y}), \qquad (4\text{-}18)$$

$$\frac{\partial u}{\partial x} + \frac{\partial v}{\partial y} = 0, \qquad (4\text{-}19)$$

where $\nu^* = \nu + \nu_t$.

In the present work the velocity-vorticity form of the Navier-Stokes equations was used, as the algorithm forming the basis for the model was formulated in velocity-vorticity variables (Shen and Phuoc, 1997). Furthermore, the equations were formulated in curvilinear coordinates, but are not presented here.

Turbulence modelling

The turbulence model used here was the one equation model of Baldwin and Barth (1990), which is derived from the classical k-ε model. The model solves a partial differential equation for the turbulent Reynolds number $R_t=k^2/(\nu\varepsilon)$, where the eddy viscosity is defined as $\nu_t=c_\mu \nu R_t D_1 D_2$, c_μ is a constant and D_1 and D_2 are damping functions. The boundary condition for R_t at the wall was taken equal to zero and at the inflow boundary it was put equal to 0.5.

4.2 Results

In order to analyse the influence of 3D rotating effects on turbulent flows, the flow past a rotating NACA 63_2-415 airfoil was computed at a Reynolds number Re=1.5x10^6. This airfoil is widely used for wind turbine rotors, e.g., the outer part of the LM 19.1 wind turbine blade. The effect of rotation was elucidated by comparing quasi-3D computations to 2D computations and measurements, with the non-dimensional spanwise distance, $k=z/c$, as additional 3D parameter. The calculations were performed on a 161x101 grid using the Baldwin-Barth turbulence model. To ensure that the first grid point off the airfoil surface was located at y^+-values less than 4, the height of the first computational cells was put equal to about 3x10^{-5} chord length.

As a first validation of the developed code, 2D computations on a 161x101 grid were compared to experimental data Abbott and Doenhoff (1959) for incidences up to 25°. The outcome is shown in Figure 4-2 in which the computed C_L-distribution is compared to measured airfoil data at a Reynolds number of 3x10^6. The comparison demonstrates that the 2D version of the code in combination with the Baldwin-Barth turbulence model was capable of predicting both stall and post-stall correctly.

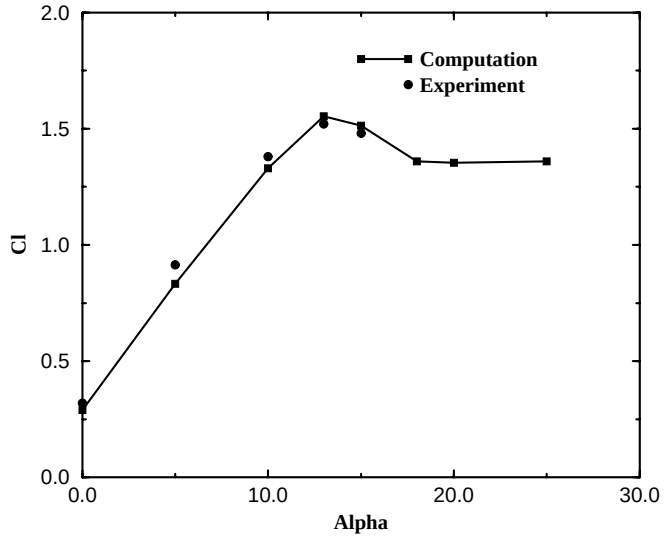

Figure 4-2 Comparison of computed 2D C_L-coefficient vs. α of a NACA 63_2-415 airfoil at Re=1.5x10^6 with experimental data at Re=3x10^6.

In order to analyse the influence of rotation on the development of separation bubbles, the flow at an incidence of 20° was studied using the quasi-3D model. In Figure 4-3, streamline plots are shown at $k=\infty$ (2D), 6 and 4.

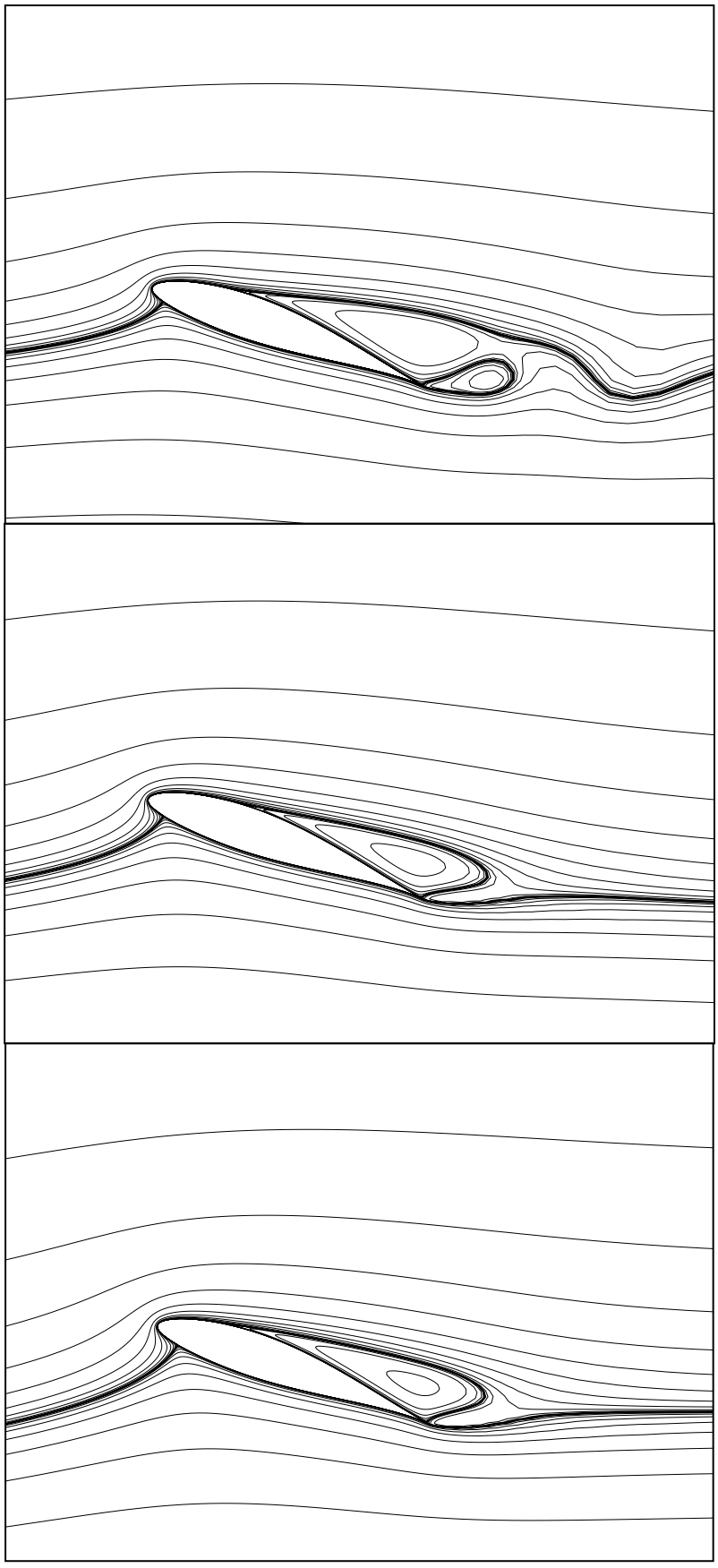

Figure 4-3 Stream lines for the flow around a NACA 63_2-415 airfoil at incidence 20° and Re=1.5x10^6, (a) 2D, (b) k=6, (c) k=4.

It is seen that the effect of rotation was to stabilise vortex shedding and suppress the growth of the separation bubble. The stagnation point moved downstream and the separation moved slightly towards the leading edge when k became small. This phenomenon is also observed in the C_p and C_f curves in Figure 4-4, in which the influence of rotation is seen to be most pronounced on the C_p-distribution.

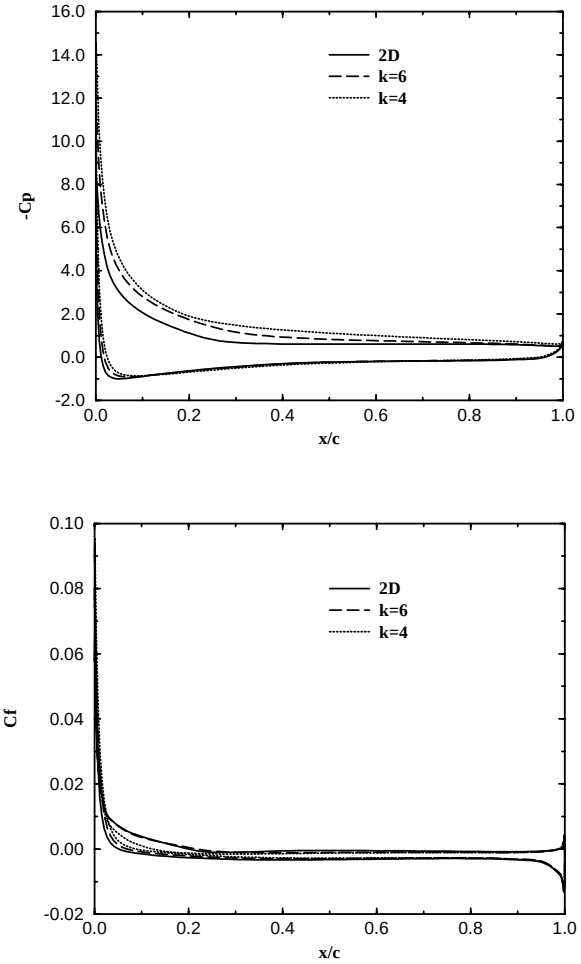

Figure 4-4 C_p and C_f distributions on a NACA 63_2-415 airfoil at incidence 20° and Re=1.5x10^6.

In Figure 4-5 we depict C_L and C_D as a function of incidence. It was observed that decreasing k, i.e., decreasing radius resulted in an increase in both C_L and C_D. Thus, a maximum C_L-value of about 1.5 in the 2D case was increased to approximately 1.9 at k=4.

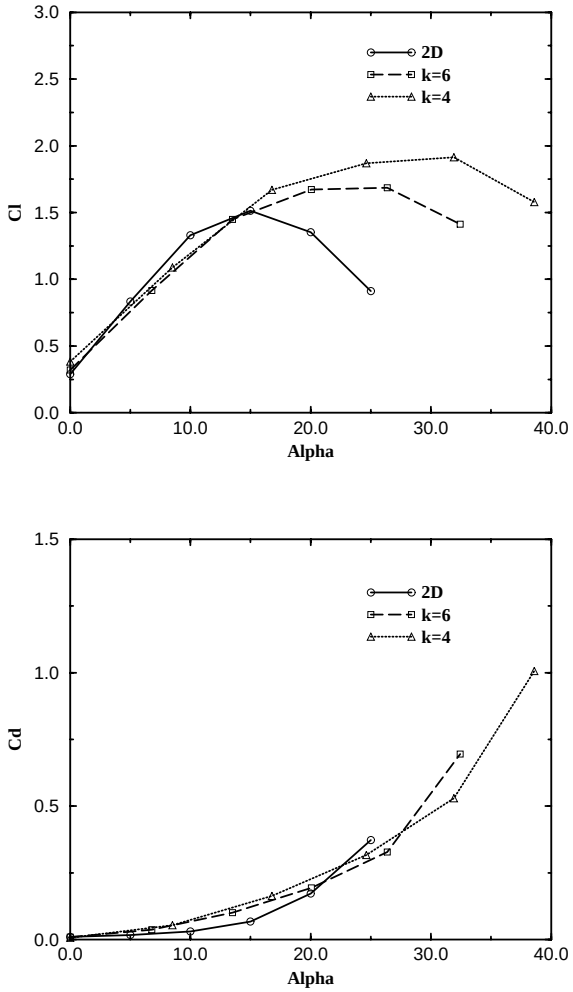

Figure 4-5 C_L and C_D vs. α of a NACA 63_2-415 airfoil at Re=1.5x10^6.

4.3 Conclusion

A quasi-3D Navier-Stokes model that took into account rotational and 3D effects was developed. The model enabled the study of the rotational effect of a rotor blade at computing costs similar to what is typical for 2D airfoil calculations.

The model showed that rotational effects had an influence on the airfoil characteristics that depended on the non-dimensional spanwise distance, $k=z/c$. Thus, the effect of rotation, which became more pronounced as the axis of rotation was approached, was to suppress vortex shedding and the development of separation bubbles. Consequently, decreasing the spanwise position resulted in an increase in both C_L and C_D.

The depicted results showed that the model was capable of determining the correct qualitative behaviour for airfoils subject to rotation. Presently the model is validated against full 3D computations in order to verify the error introduced by the basic hypothesis. If it turns out that the model gives the correct behaviour, not just qualitatively as in the cases treated here, but also quantitatively, it will be a useful tool for deriving airfoil data for use in engineering predictive codes.

5 Discussion

Four different systematic methods and the resulting airfoil characteristics have been presented in chapter 2 to 4. In the four methods, the same qualitative tendencies were reflected: High lift in stall at the inner part of the blade and low C_L in stall at the outer part of the blade compared to 2D airfoil characteristics. However, the airfoil characteristics derived by the different methods were not identical. This was due to differences in blade geometry and the different methods for deriving the data.

Airfoil characteristics for the LM 19.1 blade on a 41-m rotor based on 3D CFD were presented in section 2.3 using the actuator disc/inverse BEM method and in section 3.2 using numerical optimisation. The same tendencies for C_L were seen for the airfoil characteristics derived for both methods. However, C_L and in particular C_D were over-predicted with the numerical optimisation compared to the inverse BEM method. This was probably due to the input for the numerical optimisation, in which integral values were used: power, thrust and flap moments at five different stations on the blades. These values did not contain sufficient information about the force distributions on the blades to an unambiguous determination of C_L and C_D. Thus, the numerical optimisation resulted in airfoil characteristics, which gave the correct power, thrust and flap moment, but not necessarily the correct force distribution on the blades. Concerning the actuator disc/inverse BEM method the airfoil characteristics were believed to be accurate since the methods are based on the force distribution and not integral values such as moments. However, the inverse BEM method was based on some assumptions such as a tip correction model and an induction correction model at low wind speeds. These models should be identical to the models used in the implemented BEM model in the aeroelastic code for which the airfoil characteristics should be used.

Aeroelastic calculations with the corrected airfoil characteristics for the LM 19.1 blade derived using inverse BEM method showed that the loads were reduced with up to 15% compared to calculations with data, which are commonly used for this rotor. To verify whether the data derived from 3D CFD or the commonly used data are correct requires an analysis of measured loads on tower, nacelle etc. This analysis was not carried out in this work.

Airfoil characteristics for the LM 19.0 blade on a 41-m rotor based on measurements were presented in section 3.3. Since the derivation of these airfoil characteristics was based on numerical optimisation and thereby on measured integral values the same considerations must be carried out as for the LM 19.1 blade. Thus, the correct power and flap moments were calculated when using the derived airfoil characteristics. However, edge moments and thrust were in general not correct, since they were not measured and therefore not used in the derivation of the airfoil characteristics.

Airfoil characteristics derived by quasi-3D CFD and presented in section 4.2 gave a very useful picture of the effect of 3D flow and rotation. The derived data were presented for $k=z/c=4$ and $k=6$ corresponding to $r=6.25$ m and $r=8.5$ m, respectively, on a LM 19.1 blade for a 41-m rotor. Thus, the airfoil section NACA 63-415 used in the computations did not correspond to the selected radii.

However, comparing identical airfoil sections at different radii showed the effect of rotation and 3D flow. This gave a picture of the mechanisms underlying airfoil characteristics for rotating airfoils.

The present work has given useful qualitatively information on systematic derivation of airfoil characteristics for wind turbines as well as quantitatively information. Furthermore, the work has put focus on the uncertainties in the derivation of airfoil characteristics as well as in the use of the airfoil characteristics. Development of the methods for deriving data is necessary to obtain a better quality of the airfoil characteristics.

6 Conclusion

Each chapter of this report contains a description of the work and some conclusions of the work. From these conclusions some general conclusions on the investigated systematic methods can be drawn:

- Rotational and 3D effects on a rotor are important,
- Compared to 2D wind tunnel measurements the results show that:
  - The lift coefficient is low in stall at the tip,
  - The lift coefficient is high in stall at the inner part of the blade,
- Airfoil characteristics derived by momentum/actuator disc theory and numerical optimisation can reproduce both power and loads,
- CFD computations on a full-scale rotor show promising results with deviation from power measurements below 10 %,
- Airfoil characteristics derived by the inverse BEM method and the actuator disc method are in good agreement,
- Based on measured power and loads on a rotor the numerical optimisation method is promising since a set of C_L and C_D curves is derived that can be used to calculate mean values of power and loads. In particular the power curves were well calculated by use of the optimised airfoil characteristics.
- A quasi-3D Navier-Stokes model that takes into account rotational and 3D effects has been developed. The model enables the study of the rotational effect of a rotor blade at computing costs similar to what is typical for 2D airfoil calculations. The depicted results show that the model is capable of determining the correct qualitative behaviour for airfoils subject to rotation.

References

Abbott, I.H, and Doenhoff, E.v., 'Theory of Wing Sections', Dover Publications, Inc., New York (1959)

Andersen, P.S., Krabbe, U., Lundsager, P. and Petersen, H., 'Fundamentals of Wind Turbine Calculation (in Danish)', Risø-M-2153(rev.), Risø National Laboratory, Denmark (1980).

Bak, C. (ed.), Petersen, H., 'Blade Profile Coefficients C_L and C_D. From the unpublished report: Benchmark Tests on Power Curve Computations on Wind

Turbines – a Compendium', Risø-I-1369(EN), Risø National Laboratory, Roskilde, Denmark, December (1998).

Baldwin, B. S. and Barth, T. J., 'A one-equation turbulence transport model for high Reynolds number wall-bounded flows', NASA-TM-102847, (1990).

Bruining, A., van Bussel, G.J.W., Corten, G.P. and Timmer, W.A., 'Pressure distribution from a wind turbine blade; field measurements compared to 2-dimensional wind tunnel data', Technical Report IW-93065R, Delft University of Technology, Institute for Wind Energy, (1993).

Cebeci, T., 'Calculation of three-dimensional boundary layers I. Swept infinite cylinders and small cross flow', AIAA J., **12** (6), pp. 779-786, (1974).

de Boer, C., A Practical Guide to Splines, Springer-Verlag. New York, (1978).

FIDAP Users Manual, Revision 6.0, Theoretical Part, April, (1991).

Fogarty, L.E., 'The laminar boundary layer on a rotating blade', J. AeroSci., vol. 18, no. 4, pp. 247-252, September, (1951).

Fogarty, L. E. and Sears, W. R., 'Potential flow around a rotating, advancing cylindrical blade', J. AeroSci., vol. 17, no. 9, p. 599, September, (1950).

Fuglsang, P., Antoniou, I., Dahl, K.S. and Madsen, H.A., 'Wind Tunnel Tests of the FFA-W3-241, FFA-W3-301 and NACA 63-430 Airfoils', Risø-R-1041(EN), Risø National Laboratory, Denmark (1998)

Fuglsang, P., Madsen, H.A., 'Optimization Method for Wind Turbine Rotors', J. Wind Engineering and Industrial Aerodynamics, 80, pp. 191-206, (1999).

Hansen, M.O.L., Sørensen, J.N., Michelsen, J.A., and Sørensen, N.N., 'A Global Navier-Stokes Rotor Prediction Model', AIAA Paper 97-0970, (1997).

Hansen, M.O.L., Øye, S., Generation of 2-D airfoil data for the BEM model, (In Danish) Project note, Institute of Energy Technology, Danish Technical University (1998).

Himmelskamp, H., 'Profile investigations on a rotation airscrew', Technical Report Ph. D., Dissertation, Göttingen, (1945).

Khosla, P.K. and Rubin, S.G., 'A diagonally dominant second-order accurate implicit scheme', Computers Fluids, 2:207-209, (1974).

Madsen, H.A., 'A CFD Analysis of the Actuator Disc Flow compared with Momentum Theory Results', Proceedings of the 10th Symposium on Aerodynamics of Wind Turbines, held in Edinburgh, December 16-17, (1996).

McCroskey, W.J., 'Measurements of boundary layer transition, separation and streamline direction on rotating blades', NASA-TN-D-6321, April, (1971).

Menter, F.R., 'Performance of Popular Turbulence Models for Attached and Separated Adverse Pressure Gradient Flows', AIAA Journal, 30(8):2066-2072, August, (1992).

Menter, F.R., 'Zonal Two Equation k-ω Turbulence Models for Aerodynamic Flows', AIAA-paper-932906, (1993).

Michelsen, J.A., 'Basis3D - a Platform for Development of Multiblock PDE Solvers', Technical Report AFM 92-05, Technical University of Denmark, (1992).

Michelsen, J.A., 'Block structured Multigrid solution of 2D and 3D elliptic PDE's', Technical Report AFM 94-06, Technical University of Denmark, (1994).

Milborrow, D.J. and Ross, J.N., 'Airfoils characteristics of rotating blades', IEA LS-WECS, 12th Meeting of Experts, Copenhagen, (1984).

Patankar, S.V. and Spalding, D.B., 'A Calculation Procedure for Heat, Mass and Momentum Transfer in Three-Dimensional Parabolic Flows', Int. J. Heat Mass Transfer, 15:1787, (1972).

Paulsen, U.S., 'Konceptundersøgelse Nordtank NTK 500/41. Strukturelle laster (In Danish)', Risø-I-936(DA), Risø National Laboratory, Roskilde, Denmark, November, (1995).

Petersen, J.T., 'The Aeroelastic Code HawC – Model and Comparisons', In proc. State of the Art of Aeroelastic Codes for Wind Turbine Calculations, 28th Meeting of Experts, International Energy Agenscy, Annex XI, Editor B. Maribo Pedersen, Technical University of Denmark, pp. 129-135, April 11-12, (1996).

Petersen, J.T. and Madsen, H.A., 'Local Inflow and Dynamics – Measured and Simulated on a Rotating Wind Turbine Blade', Risø-R-993(EN), Risø National Laboratory, Roskilde, Denmark, April (1999).

Radwan, S.F. and Lekoudis, S.G., 'Boundary layer calculations in the inverse mode for incompressible flows over infinite swept wings', AIAA J., **22** (6), pp. 737-743, (1984).

Rasmussen, F., 'Blade and rotor loads for Vestas 15', Risø-M-2402, Risø National Laboratory, Roskilde, Denmark (1983).

Rhie, C.M., 'A numerical study of the flow past an isolated airfoil with separation', PhD thesis, Univ. of Illinois, Urbane-Champaign, (1981).

Ronsten, G., 'Static pressure measurements on a rotating and a non rotating 2.375 m wind turbine blade - comparison with 2D calculations', Amsterdam EWEC '91, 214-220, Elsevier Science Publishers B. V., (1991).

Savino, J.M. and Nyland, T.W., 'Wind turbine flow visualisation studies', Technical report, NASA Lewis Research Center, Cleveland, Ohio, (1985).

Schepers, J.G., Brand, A.J., Bruining, A., Graham, J.M.R., Paynter, R.J.H., Hand, M.M., Simms, D.A., Madsen, H.A., Infield, D.G., 'Final Report of IEA Annex XIV: Field Rotor Aerodynamics', Report ECN-C-97-027, ECN, (1997)
Sears, W. R., 'Potential flow around a cylindrical blade', Journal of the Aeronautical Sciences, vol. 17, no. 3, pp. 183-184, (1950).

Shen, W. Z. and Phuoc, L. Ta, 'Numerical method for unsteady 3D Navier-Stokes equations in velocity-vorticity form', Computer & Fluids, Vol. 26, No. 2, pp. 193-216, (1997).

Smith, P., 'Aerodynamic Theory: A General Review of Progress – Vol. IV. Applied Airfoil Theory, Etc.', Peter Smith Publisher, Inc. (1976).

Snel, H., Houwink, R., Piers, W.J., Bosschers, J., van Bussel, G.J.W. and Bruining, A., 'Sectional prediction of 3D effects for stalled flow on rotating blades and comparison with measurements', Lübeck Travemünde EWEC '93, pp. 395-399, H. S. Stephens & Associates, March, (1993).

Sørensen, D.N. and Sørensen, J.N, 'Quasi-3D model for rotating airfoil', 13th AIAA Applied Aerodynamic Conf., Santiago, AIAA paper 95-1916, (1995).

Sørensen, J.N., 'Three-level viscous-inviscid interaction technique for the prediction of separated flow past rotating wings', AFM Report 86-07, Department of Fluid Mechanics, Technical University of Denmark, (1986).

Sørensen, N.N., 'General Purpose Flow Solver Applied to Flow over Hills', Risø-R-827(EN), Risø National Laboratory, Roskilde, Denmark, June, (1995).

Wilcox, D.C., 'Turbulence Modeling for CFD',DCW Industries, Inc., La Canada, California, 2 edition, November, (1994).

Øye, S., FLEX4 Simulation of Wind Turbine Dynamics, Proc. 28th Meeting of Experts, International Energy Agency, Annex XI, pp. 71-77, (1996).

Bibliographic Data Sheet **Risø-R-1065(EN)**

Title and authors

Airfoil Characteristics for Wind Turbines

Christian Bak, Peter Fuglsang, Niels N. Sørensen, Helge Aagaard Madsen
Risø National Laboratory
Wen Zhong Shen, Jens Nørkær Sørensen
Technical University of Denmark

ISBN
87-550-2415-7
87-550-2568-4 (internet)

ISSN
0106-2840

Department or group
Wind Energy and Atmospheric Physics Department

Date
March 1999

Groups own reg. number(s)
1110015-00

Project/contract No(s)
ENS 1363/97-0002
ENS 1363/98-0005

Pages	Tables	Illustrations	References
51	2	52	42

Abstract (max. 2000 characters)

Airfoil characteristics for use in the Blade Element Momentum (BEM) method calculating the forces on Horizontal Axis Wind Turbines (HAWT) are derived by use of systematic methods. The investigation and derivation of the airfoil characteristics are based on four different methods: 1) Inverse momentum theory, 2) Actuator disc theory, 3) Numerical optimisation and 4) Quasi-3D CFD computations.

The two former methods are based on 3D CFD computations and wind tunnel measurements on a 41-m full-scale rotor with LM 19.1 blades. The derived airfoil characteristics show that the lift coefficient in stall at the tip is low and that it is high at the root compared to 2D airfoil characteristics. The use of these characteristics in aeroelastic calculations shows a good agreement in power and flap moments with measurements. Furthermore, a fatigue analysis shows a reduction in the loads of up to 15 % compared to a commonly used set of airfoil characteristics.

The numerical optimisation is based on both the 3D CFD computations and measurements on a 41-m rotor with LM 19.1 and LM 19.0 blades, respectively. The method requires power and loads from a turbine and is promising since a set of lift and drag curves is derived that can be used to calculate mean values of power and loads. The lift in stall at the tip is low and at the root it is high compared to 2D airfoil characteristics. In particular the power curves were well calculated by use of the optimised airfoil characteristics.

In the quasi-3D CFD computations, the airfoil characteristics are derived directly. This Navier-Stokes model takes into account rotational and 3D effects. The model enables the study of the rotational effect of a rotor blade at computing costs similar to what is typical for 2D airfoil calculations. The depicted results show that the model is capable of determining the correct qualitative behaviour for airfoils subject to rotation. The method shows that lift is high at the root compared to 2D airfoil characteristics.

The different systematic methods show the importance of rotational and 3D effects on rotors. Furthermore, the methods show high lift coefficients in stall at the inboard part of the blade and low lift coefficients in stall at the outboard part of the blade compared to 2D wind tunnel measurements.

Descriptors INIS/EDB

AERODYNAMICS; AIRFOILS; COMPUTATIONAL FLUID DYNAMICS; COMPUTER CALCULATIONS; HORIZONTAL AXIS TURBINES; NAVIER-STOKES EQUATIONS; ROTORS; THREE DIMENSIONAL CALCULATIONS; TURBINE BLADES

Available on request from Information Service Department, Risø National Laboratory,
(Afdelingen for Informationsservice, Forskningscenter Risø), P.O.Box 49, DK-4000 Roskilde, Denmark.
Telephone +45 46 77 40 04, Telefax +45 46 77 40 13